SAND2019-6674

SANDIA REPORT

SAND2019-214278

Printed April 2019

Sandia National Laboratories

Active Dopant Optical Spectroscopy via Laser Ablation for High Resolution Spectral Measurements

Sonal Patel and Sean Simpson

Prepared by
Sandia National Laboratories
Albuquerque, New Mexico 87185
Livermore, California 94550

Issued by Sandia National Laboratories, operated for the United States Department of Energy by National Technology & Engineering Solutions of Sandia, LLC.

ABSTRACT

The goal of this exploratory express LDRD is to demonstrate a reproducible laser activated doping diagnostic for eventual use on the Z machine by producing consistent spectral line emission with radiances above 10^5 $\mathrm{W\,sr^{-1}\,nm^{-1}\,m^{-2}}$ from a variety of dopant materials. Here we show that while such radiances are achieved, the line emission is from regions with high electron densities, and close to the laser ablation surface. Therefore, it would be more ideal to improve current optical spectroscopy capabilities on Z to view radiances around 10^4 $\mathrm{W\,sr^{-1}\,nm^{-1}\,m^{-2}}$. We also discuss the viability of a modular beam path that can be remotely aligned and used on the Z machine. This technique can be used to make spatially resolved measurements of electric and magnetic field strengths and electron densities within the Z power flow and load regions. The measurements can also be used to inform theory and simulation efforts needed to design the next generation of pulsed power capabilities.

This was funded as an exploratory LDRD project, number: 214278

ACKNOWLEDGMENT

Thanks to Dan Scoglietti, who helped align the beam and take some of this data. Thanks also to Dave Bliss for discussions on optics and lasers, Keven MacRunnels who helped set up the lab, Mark Johnston for the dopant related discussions, George Laity for his continued support in this diagnostic, and Mike Cuneo for suggesting the diagnostic technique in the first place.

CONTENTS

LIST OF FIGURES

LIST OF TABLES

1. INTRODUCTION

Currently, passive dopant optical spectroscopy on the Z-machine is used to measure plasma formation within the magnetically insulated transmission lines (MITLs). Passive dopants use the Z pulse to ablate the dopant material and line intensities from these dopants have often been too weak during relevant time scales to make meaningful measurements on plasma parameters.

Here, we discuss active doping techniques that use a laser to ablate material and produce a low density plasma at a specific time. Changes in the line shapes from these materials can be used to infer electron densities, temperatures, electric and magnetic fields during the pulse. Improved line intensity at a controlled time would lead to high resolution measurements necessary to estimate plasma parameters and field strengths in a variety of locations both near the load and within power flow regions, which can help inform simulation efforts for the next generation of pulsed power capabilities.

In this report, we measure line emission from several dopant materials and spectral lines. We estimate electron densities from various dopant materials at several times after the laser pulse and at several distances from the laser ablation surface. We also estimate electron temperatures using Li I line ratios. In order to field such a diagnostic on Z, beam alignment cannot be time consuming and the laser must be fully enclosed, so we also discuss techniques that can be used to achieve final alignments quickly using remotely controlled mirrors and shutters.

2. EXPERIMENTAL SETUP

2.1. Laser Setup

A Tempest 10 Hz, 1064 nm, Nd:YAG laser is used to ablate material off of a 304 stainless steel disk. The laser has a 5 ns pulse width, operated at 2 Hz during alignments, but switched to single pulse mode for spectral measurements of the ablation plasma. The layout is shown in Figure 2-1 and a picture of the setup is given in 2-2

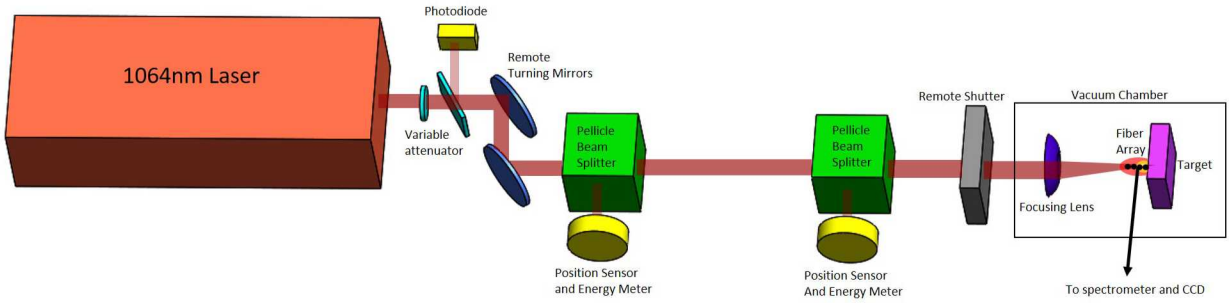

Figure 2-1. Schematic showing the laser beam path and optical elements.

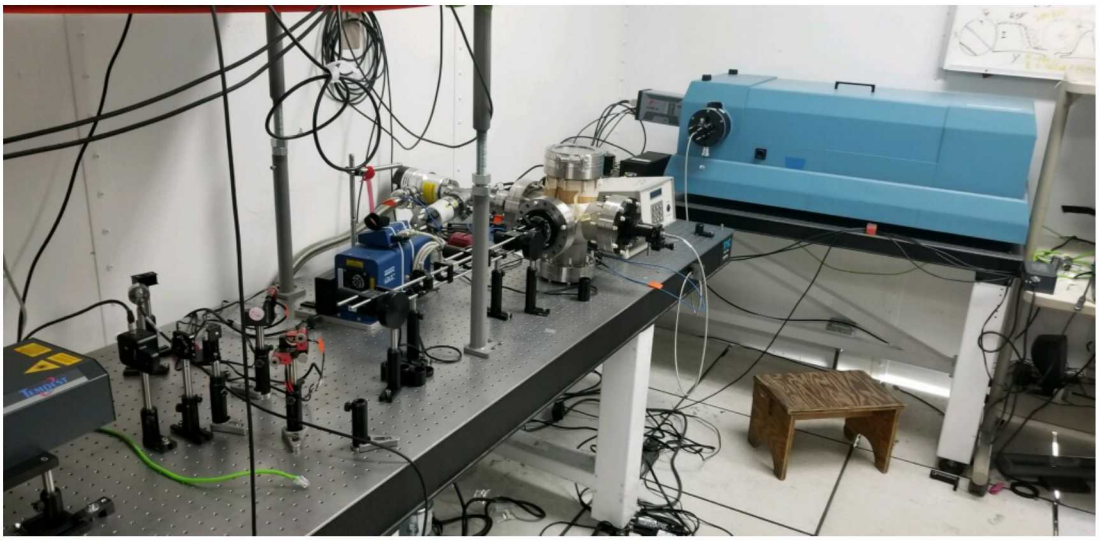

Figure 2-2. Picture of the beam path, spectrometer, and ICCD camera.

The approximately 5 mm beam exits the laser and passes through an external variable attenuator which consists of a $1/2$ waveplate and plate polarizer. A portion of the discarded beam is measured with a photodiode, which provides timing information. Two turning mirrors align the beam remotely. Two pellicle beam splitters pick off a few percent of the beam energy at 90 degrees which is relayed to an energy meter and quad diode sensor, as shown in Figure 2-1. The quad diode comprises the position sensing detector, allowing for remote alignment of the beam to the optical axis of the optical train and experiment. The beam is aligned to the center of the quad diode (positioned at 90 degrees to the optical axis). A remote shutter, just before the final focusing lens, is used to align the beam without ablating the target material. Once alignments are completed, the laser is switched to single shot mode, and the shutter is opened. The beam passes into a vacuum chamber where a lens focuses the beam onto the target.

Because a fully enclosed laser beam and fast alignments are important for fielding an active dopant diagnostic on the Z-machine, this alignment system is designed to be modular and enclosed (although it was run as an open beam for the purposes of this EE LDRD). The variable attenuator and two turning mirrors can be placed in an optical enclosure. The beam splitters and position sensors can be entirely enclosed with standard 1" beam tubes, and bolted onto the laser and vacuum chamber. Alignments are done remotely using two piezo motor mirror mounts. Rough alignments can be accomplished in a light lab. The parts can then be decoupled, moved, and reattached, without much change in the beam position. As long as the beam shift due to small changes in the mirror positions or the laser pointing, is less than 5 mm on the second pellicle beam splitter (which corresponds to about 0.5 degrees for this test setup), alignments can be finalized within a few minutes. A third position sensor may also be added between the two in cases where a particularly long beam path allows for much less beam shift.

Typically, the laser is used without post spatial filtering as this is the simplest system geometry. However, in order to improve beam quality and increase the deposited energy density, a 200 μm spatial filter (at atmosphere) was also fielded on a subset of the data. This is discussed in more

detail in the following sections.

Ideally, a short focal length lens would have been used to focus the beam onto the target to minimize the spot size and maximize the fluence. However, these measurements were taken with a longer focal length, 55 mm, lens in order to increase the lens-to-target distance to prevent coating the lens with dopant and target materials, particularly under vacuum. In this configuration, the diffraction limited spot size at the target was much larger since a beam expander was not used to increase the beam diameter at the final lens. For single shot measurements such as those that are proposed for Z, an improved lens design could be employed which would benefit from a shorter focal length for the final focusing lens, which could relax the energy requirements for the laser while producing higher density plasmas.

2.2. Spectrometer and ICCD Camera

A fiber array images the ablation plume. Initially, a 100 μm fiber array was fielded, with each fiber separated by 100 μm. The array imaged a series of 0.55 mm diameter circular regions. To improve spectral signals for high resolution measurements, this array was replaced by a 7 fiber 200 μm array, which images a 1.1 mm diameter region without any spacing between the fibers. Profiles of the arrays are shown in Figure 2-3. The array is positioned normal to the target surface, so expansion of the plasma plume and plasma parameters as a function of distance from the target surface can be determined.

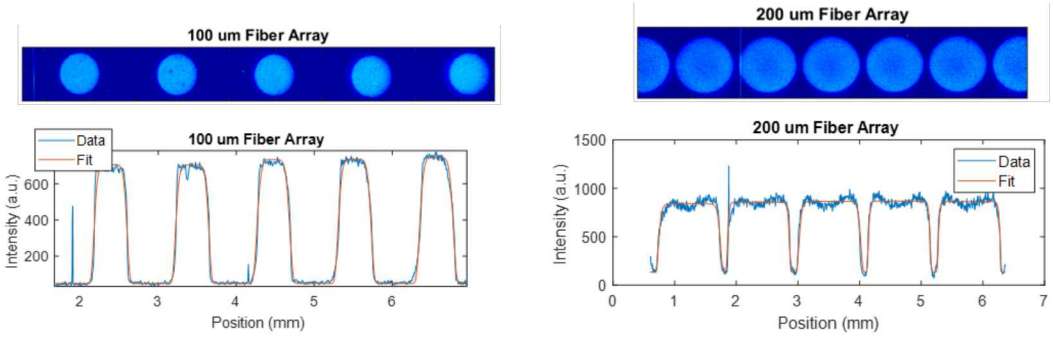

(a) Unfiltered **(b)** Filtered

Figure 2-3. a) 100 μm fiber array. Each fiber is focused to a 0.55 mm diameter. Although only five are visible on the beam profiler 10 fibers were used to image the plasma plume. b) 200 μm fiber array, focused to 1.1 mm diameters.

The array is lens coupled to a 1m McPherson spectrometer, the majority of measurements were taken on a 600 g/mm grating (0.17 nm resolution). Lower resolution measurements were also taken for temperature estimates from spectral line ratios.

The Princeton Instruments PiMax4 camera has a 1024x256 CCD array and an IR HRf coating. The quantum efficiency of this coating peaks at around 650 nm at 30%. At 400 nm the efficiency is about 7%. Using an HBf coated ICCD would increase the efficiency to 35-50% in the visible

wavelengths and improve these measurements. Streak spectroscopy on Z has shown rapidly evolving plasmas on the electrode surfaces over 5-10 nanoseconds. The ICCD was therefore gated for 3-5 ns, with a gain of 80. If the field strengths and plasma parameters evolve less rapidly further from the electrode surfaces, the ICCD could be gated for longer times to view lower density plasmas.

2.3. Calibrations

Typically SVS is fielded with a 50-150 g\mm grating, a 200ns sweep window, 100 μm fibers and a 100um spectrometer slit width. The minimum spectral radiance that can be measured on SVS at these settings is estimated to be about 10^5 $\mathrm{W\,sr^{-1}\,nm^{-1}\,m^{-2}}$ at 450-700 nm. The purpose of this LDRD is to determine peak spectral radiances of various lines that can be produced via laser ablation and determine if the line emission can be successfully measured on Z using the existing SVS systems. In order to compare the existing SVS systems and gated camera measurements, an absolute calibration must be performed.

On Z the SVS systems are calibrated by sweeping a tungsten light source over 8s. The correction from 8 seconds to several hundred nanoseconds is not linear across time and wavelength. To compensate for this, a laser driven light source (LDLS) is swept at fast (several hundred nanoseconds) and slow (8s) sweep rates. A calibrated ND filter is used to on the longer sweep rates to prevent saturation and damage to the camera. This corrects the 8s sweep of the tungsten blackbody source to shot rate settings.

A similar method is used to calibrate the ICCD camera for these measurements. The fiber array images the tungsten lamp on a 10 ms exposure. Since shot data is taken a 3-5 ns gate, the LDLS with a calibrated ND filter is again used to correct for the difference in exposure times. Wavelength and instrument resolution are estimated from an HgNe lamp. Position is estimated using the array profiles in Figure 2-3 and the tungsten lamp.

3. EXPERIMENTAL RESULTS

3.1. Low Resolution Measurements

Initially, a low resolution grating (150 g/mm, corresponding to a spectral resolution of about 0.7 nm at a 100 um spectrometer slit width) was used to estimate ablation plume electron temperatures from Li I line ratios. Spectral resolution is determined from fitting Ne lines from an HgNe pen lamp.

Spectra were taken using a 2.5 μg droplet of a 1 g/L LiCl liquid solution on a 304 stainless steel target and the LiCl dopant was replaced after every shot. Vacuum pressure was between 3×10^{-4} - 5×10^{-4} Torr. Although Z shot vacuum pressures are around mid-1×10^{-5} torr, there did not appear to be a noticeable difference between 1×10^{-4} and 1×10^{-5} Torr scales in the collected spectra, and so mid 1×10^{-4} Torr was chosen for these experiments. Since vacuum is broken to

Time (ns)	Energy (mJ)
100	110
150	111
200	110
250	110
300	110
380	110

Table 3-1. Summary of the low resolution measurements, listing the time after the laser pulse and the corresponding energy for each shot. The laser is extremely stable at these energies, allowing for cross comparisons of different shots.

replace the dopant between every ablation measurement, this allowed for much faster data collection.

Energy is measured using the first pellicle beam splitter and position/energy sensor along the laser beam path. To calibrate this measurement with the total energy reaching the target, the laser is fired at lower energy (less than 30 mJ to prevent damage to the energy meter) and measured near the target. A linear correction is applied at higher power to translate the energy measurement at the first pellicle to the laser energy that reaches the target. The low resolution measurements are charted in Table 3-1.

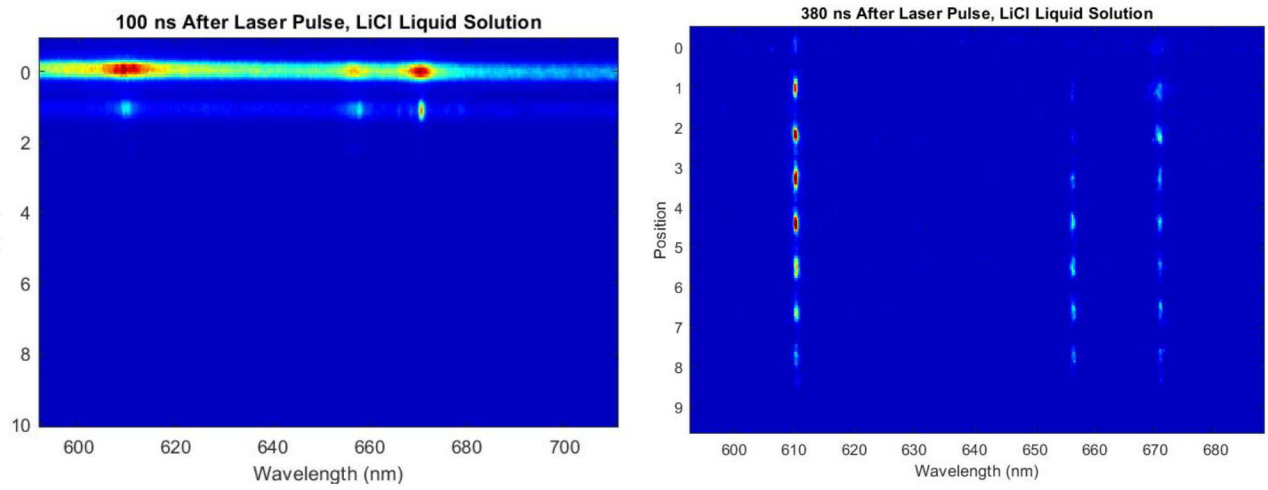

(a) 100ns **(b)** 380ns

Figure 3-1. a) 100 ns after the laser pulse. b) 380 ns after the plume, the plasma has expanded, electron densities have dropped, and clear narrow spectral lines from Li I (610.4 and 670.8 nm) and H-a are visible.

The ablation plume is measured at intervals after the initial laser pulse. And a region that extends from the surface to about 8 mm from the surface is imaged. Two example images are shown in Figure 3-1. Each chord corresponds to a fiber separated by about 1.1 mm from the center of

adjacent fibers.

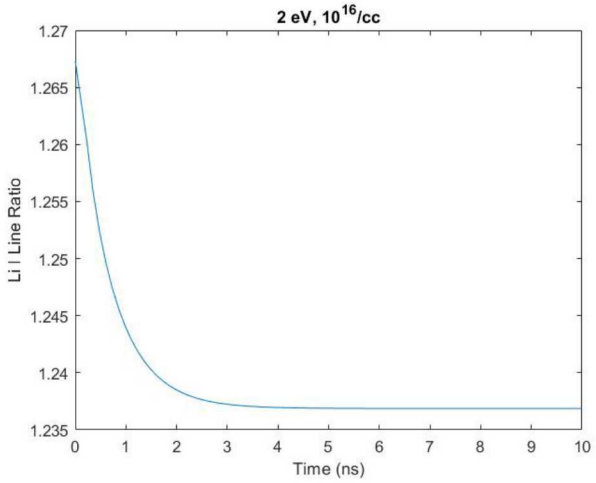

Figure 3-2. The Li I ratio equilibriates rapidly, within a few ns at this temperature and density.

Electron temperatures are estimated using PrismSPECT calculations and Li I line ratios. LTE is not assumed due to the rapidly expanding ablation plasma. Time dependent calculations, shown in Figure 3-2 suggest that the Li I line ratio reaches equilibrium within a few nanoseconds at 2 eV and 1×10^{16} cm^{-3} electron densities. As a result, an nLTE, steady-state simulation is used.

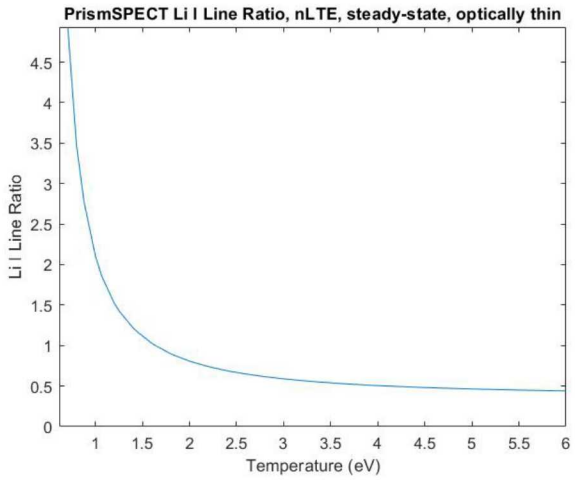

Figure 3-3. The Li I line ratio does not vary appreciably above 2 eV.

Due to the small energy difference the Li I ratio (670.8nm/610.4nm) is only useful under electron temperatures of about 2 eV (corresponding to a ratio of about 0.81). Above this, the line ratio does not vary appreciably with temperature, as shown in Figure 3-3. Line ratios between two different ions of the same species would be more useful to estimate the higher temperatures.

Figure 3-4 shows estimated line ratios and temperatures between about 0.8 and 2 eV from the Li I lines. Electron temperature tends to increase with time. A number of neutral spectral lines should

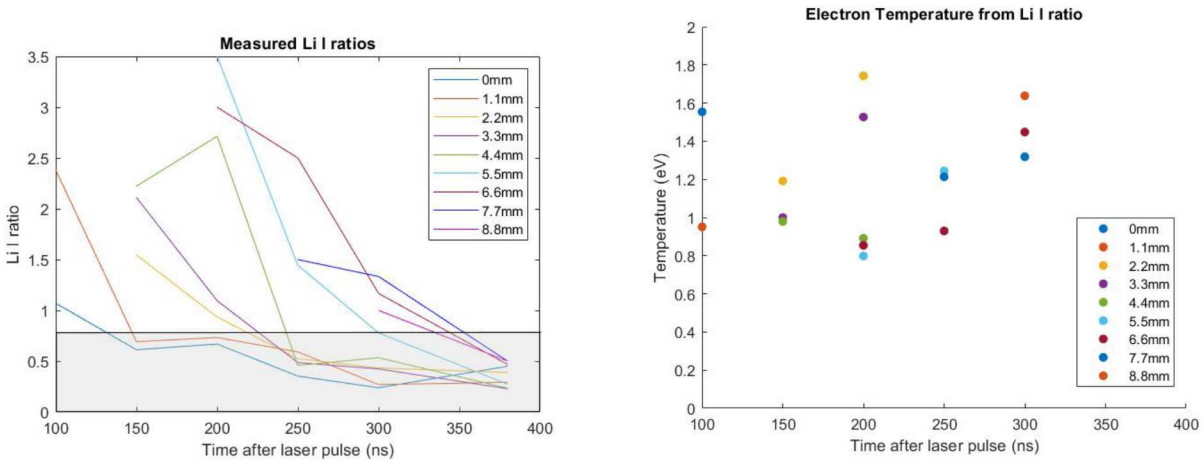

(a) Li I Measured Ratio

(b) Estimated Electron Temperature

Figure 3-4. a) Measured Li I line ratios. b) Estimated electron temperatures under 2 eV.

have sufficient peak spectral radiance at these temperatures for streak spectroscopy measurements on the Z-machine, as well as a few ion lines, such as Mg II (448.1 nm) which at an electron density of 2×10^{16} cm^{-3}, has a peak spectral radiance of 5×10^{5} W sr^{-1} nm^{-1} m^{-2}, estimated from PrismSPECT. Figure 3-5 shows peak radiances of the Li I lines as a function of temperature at an electron density of 1×10^{16} cm^{-3}.

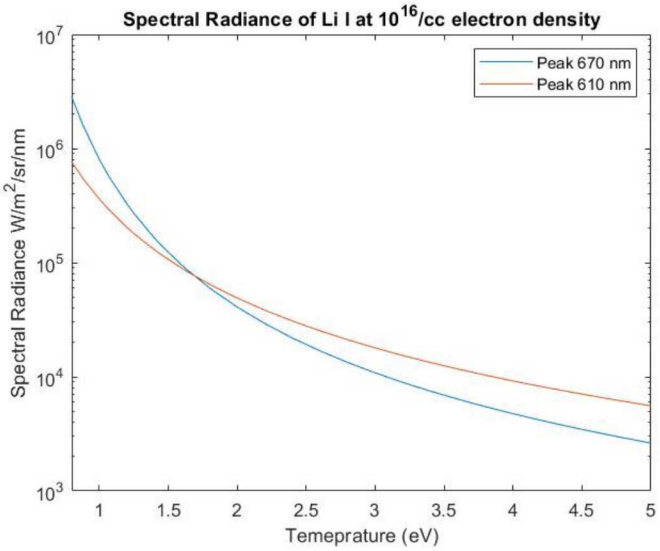

Figure 3-5. Li I spectral radiance estimated in PrismSPECT. SVS requires above greatest 10^{5} W sr^{-1} nm^{-1} m^{-2} to measure signal strengths in the visible wavelengths.

Optically thin emission is assumed here. However, this is still uncertain based on the high resolution measurements shown in Appendix A. The sodium lines, in particular clearly show the

doublet ratio is less than two for several measurements, suggesting opacity does affect these data. Another way to estimate opacity is to place a mirror behind the ablation plasma and measure the line intensity, if the line intensity is less than two then the optical depth should be determined. By ignoring opacity effects, the estimated temperatures would be too high in the case of this Li I line ratio.

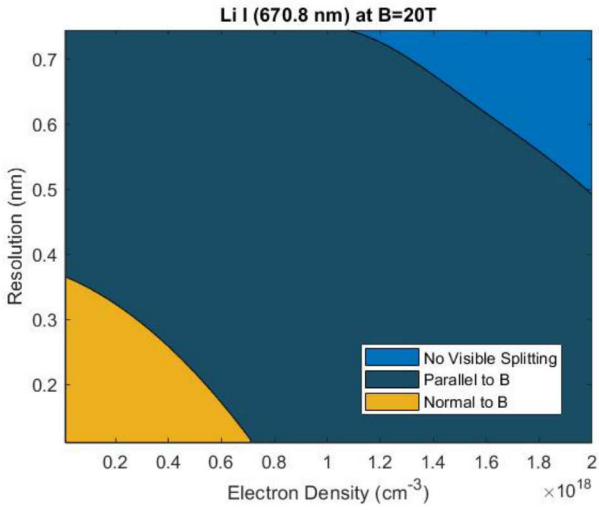

Figure 3-6. Estimated resolution requirements to resolve Zeeman splitting at a magnetic field of 20 T. Resolution requirements are lowered when viewing parallel to the B-field.

The 0.7 nm spectral resolution is inadequate for estimating electron density for the majority of measurements. Additionally, while this resolution may be sufficient for some E and B-field estimates on Z, higher resolution would provide access to lower fields and improve the accuracy of the measurement. For example, Figure 3-6 shows the resolution requirements for resolving line splitting due purely to a magnetic field of 20 T. While a resolution of 0.7 nm would be sufficient to resolve Zeeman splitting when viewing parallel to the B-field for densities below 1×10^{18} cm^{-3}, to resolve line splitting, in this case, viewing perpendicular to the B-field, the instrument resolution must be improved.

3.2. High Resolution Measurements

In order to improve the spectral resolution, the collection efficiency of the instruments must also be improved. Improving the resolution by a factor of 4 by increasing the grating density from 150 g/mm to 600 g/mm decreases the efficiency by about a factor of 4 as well. To compensate for this, the 100 um fibers were replaced with 200 um diameter fibers.

For the measurements in this section a 600 g/mm grating is used, resulting in a spectral resolution of about 0.17 nm. Additionally, the ICCD gate width is reduced from 5 ns to 3 ns. Previous measurements on Z have shown rapidly changing plasma conditions (within a few nanoseconds) on the electrode surfaces. Even shorter gate widths would be ideal, but 3 ns is at the limit of the

PiMax4 camera, and reducing the gate width would likely mean reducing the spectral resolution to compensate for the lower efficiency. Finally, a solid coating was used instead of the liquid dopant solution in Section 3.1 to more accurately reflect the measurement on Z.

Measurements are absolutely calibrated for spectral radiance, using the technique described in 2.3. Energy per shot ranges from about 105-115 mJ. All fitted data, the average stark widths, and the peak spectral radiance are shown in Appendix A. For the case of multiplet lines, only the peak intensity is shown. For some lines, particularly within 100-200 ns after the laser pulse and within 2 mm of the target surface, an additional high density component is used to fit the outer "wings" of the line. Only the average densities are tabulated.

The lines are fit with a Voigt profile. The instrument resolution of 0.165 nm comprises the Gaussian portion. At this resolution, a 0.03 nm Lorentzian FWHM contribution to the Voigt profile increases the total line width by about 10%. Therefore, Lorentzian components below 0.03 nm FWHM are not used to estimate density, as the spectral line width is too close to the instrument resolution.

3.2.1. Li I

Li I was measured from a LiF coated 304 stainless steel disk. The coating was 0.5 microns thick. The 1s2p-1s2s Li I transition is of interest for B-field measurements. The small fine structure energy separation would place it in the Paschen-Back regime for expected B-fields on Z. The Li I 1s3s-1s2p transition is sensitive to electric fields, and has been used to measure E-fields in ion diodes [1]. Here, measurements of Li I (1s2p-1s2s) are shown. Li I lines have also been measured on Z both in absorption and emission.

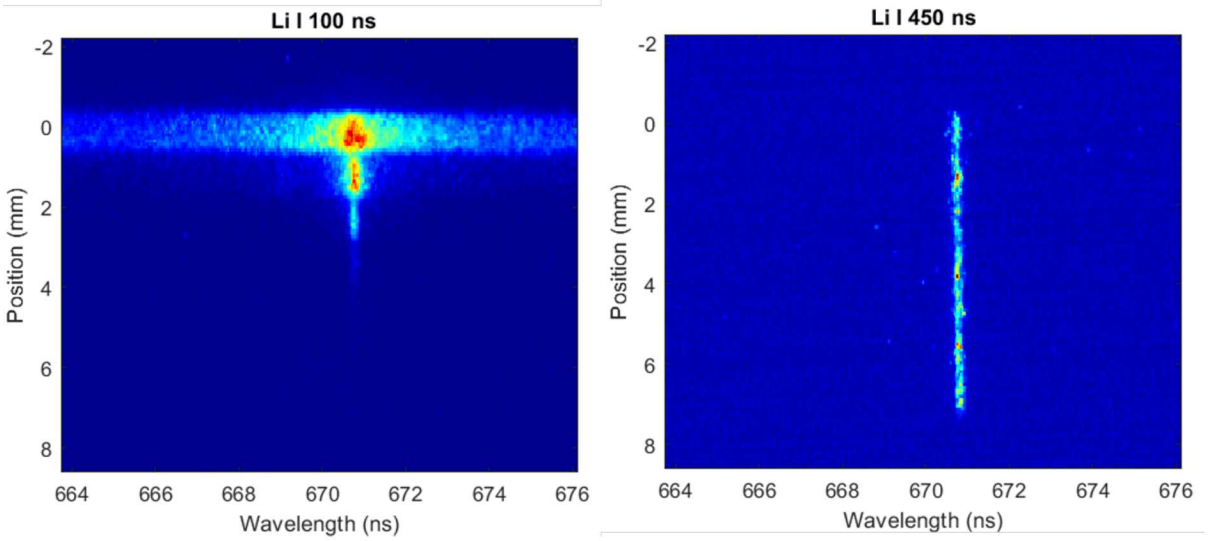

Figure 3-7. Calibrated data at 100 ns and 450 ns after the laser pulse

The laser energy was about 105 mJ for these Li I measurements. Spectral radiance is above 10^5 $\mathrm{W\,sr^{-1}\,nm^{-1}\,m^{-2}}$ only at 100-150 ns after the laser pulse and within 3 mm from the target. The lines are very broad at these times and locations. Furthermore, increasing the laser fluence will

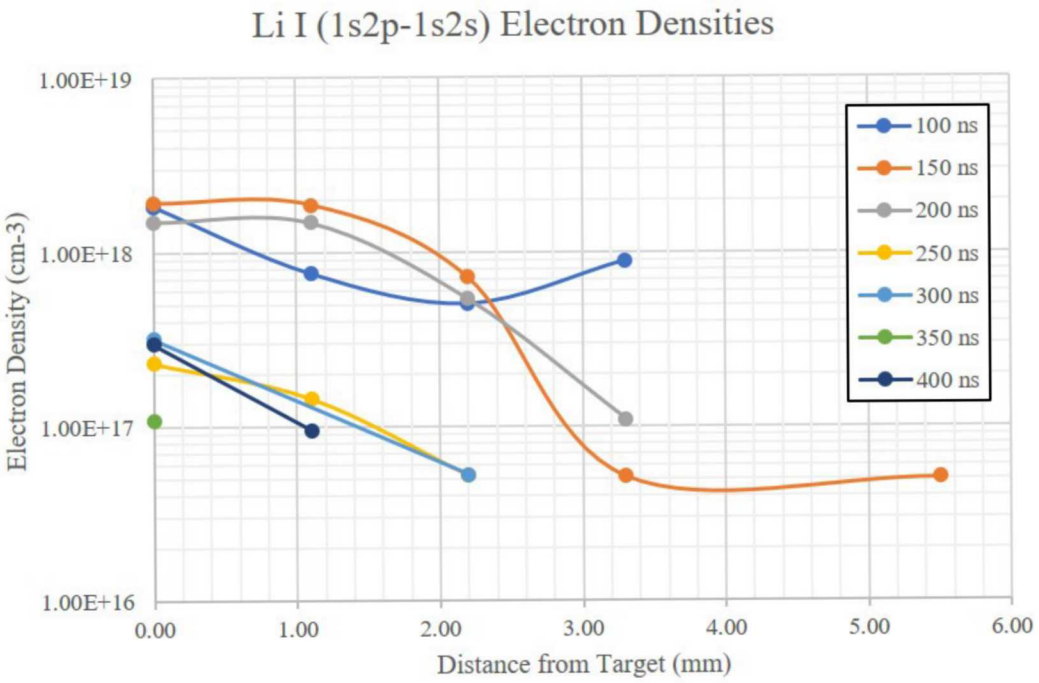

Figure 3-8. Estimated electron densities from the Li I 1s2p-1s2s line using Stark widths from [2].

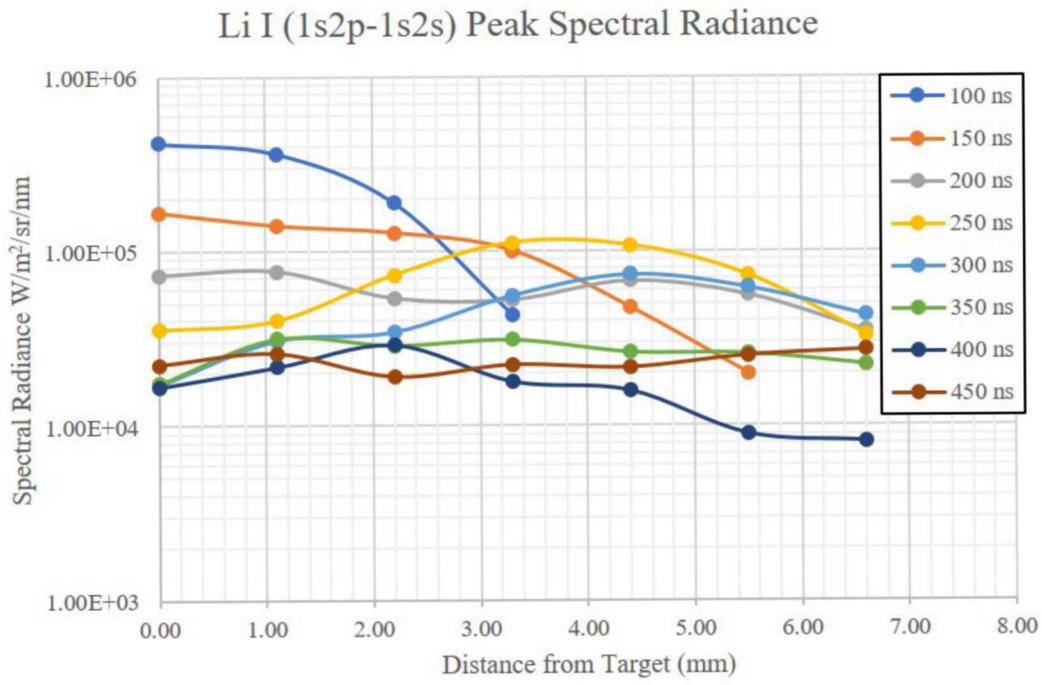

Figure 3-9. Peak Spectral Radiance

increase the electron densities. In this case, the efficiency of SVS should be improved to view the lower density regions.

Li I is the lightest atom tested here, and consequently the Li plasma expands faster than the Mg, Na, or Cu doped plasma. Within 200 ns the plasma has expanded to at least 6.6 mm. Stark widths in this region are less than 0.03 nm, which correspond to electron densities less than 4×10^{16} cm^{-3}.

3.2.2. Na I

The Na I (2p3p-2p3s) doublet is a strong line that has been measured on Z both as an applied and accidental dopant in absorption. This particular transition has been used to infer B-fields on Z in [5]. For these measurements Na I was measured from an NaCl, 0.5 micron coating on 304 stainless steel. Laser energies were about 115 mJ. Electron densities remained fairly low, peaking at around 6×10^{17} cm^{-3}. Expansion velocities are expected to be less for a sodium plasma than the lithium plasma, and so spectral radiance measurements do not extend to 6.6 mm until about 350 ns. As with the Li I measurements, Na I is measured at sufficient spectral radiance for SVS at early times and close to the target surface.

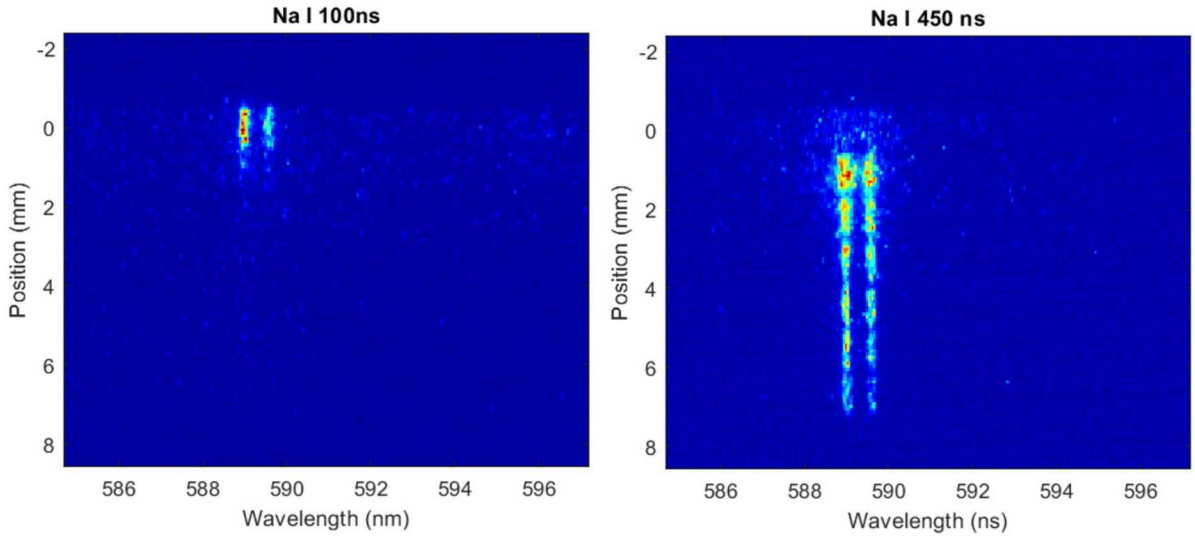

Figure 3-10. Calibrated data at 100 ns and 450 ns after the laser pulse

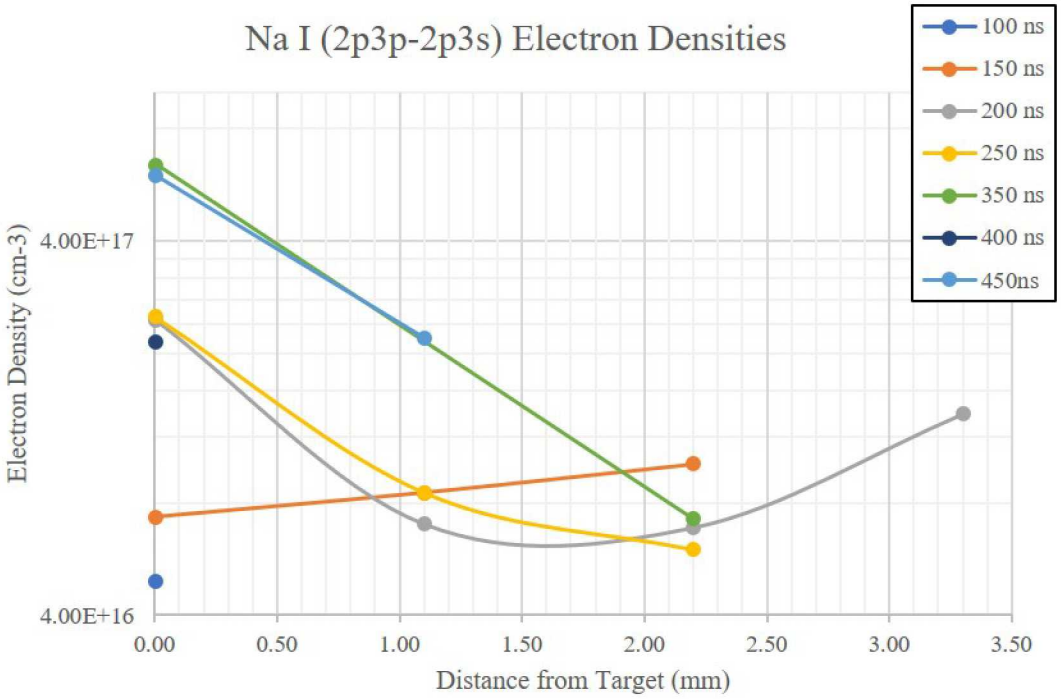

Figure 3-11. Estimated electron densities from the Na I (2p3p-2p3s) line using Stark widths from [3].

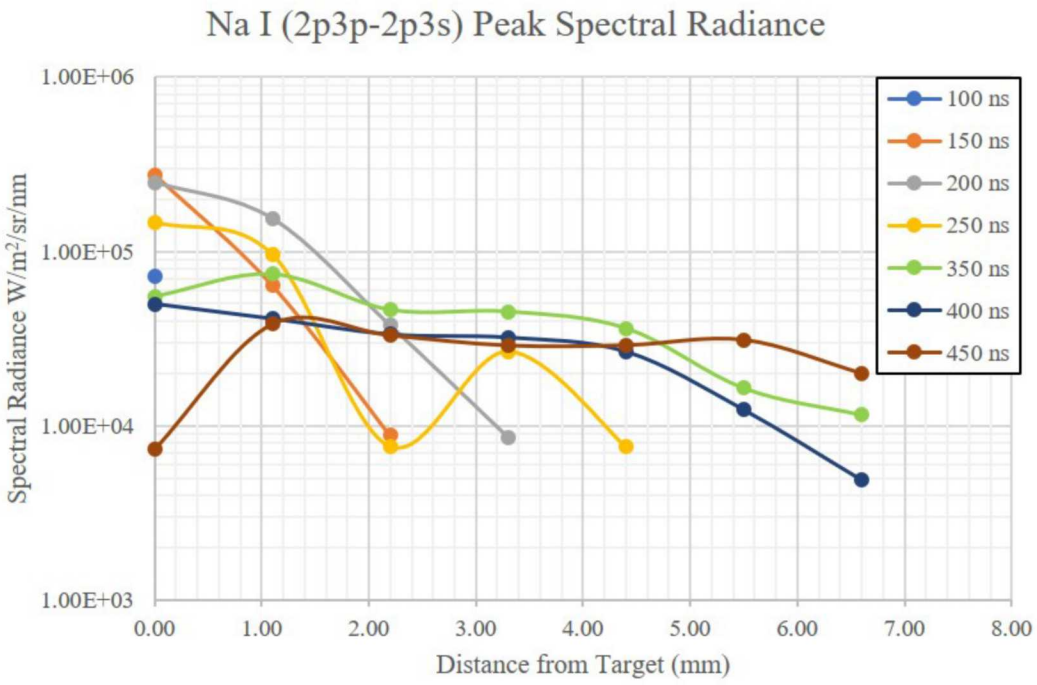

Figure 3-12. Peak Spectral Radiance

3.2.3. Mg I

Mg I (3s4s-3s3p) may not be ideal for measurements of B or E-fields since the closely spaced triplet may complicate measurements of the line shifts/splits. However, the line has been measured on Z in absorption at saturation or close to saturation levels. Additionally, it may be useful for estimates of electron temperature since the Mg II line at 448.1 nm is roughly the same intensity as the Mg I triplet at 518.3 by 1 eV, and the Mg II/Mg I ratio continues to increase with temperature. The plots shown here are from a MgF2, 0.5 um coating on a 304 stainless surface.

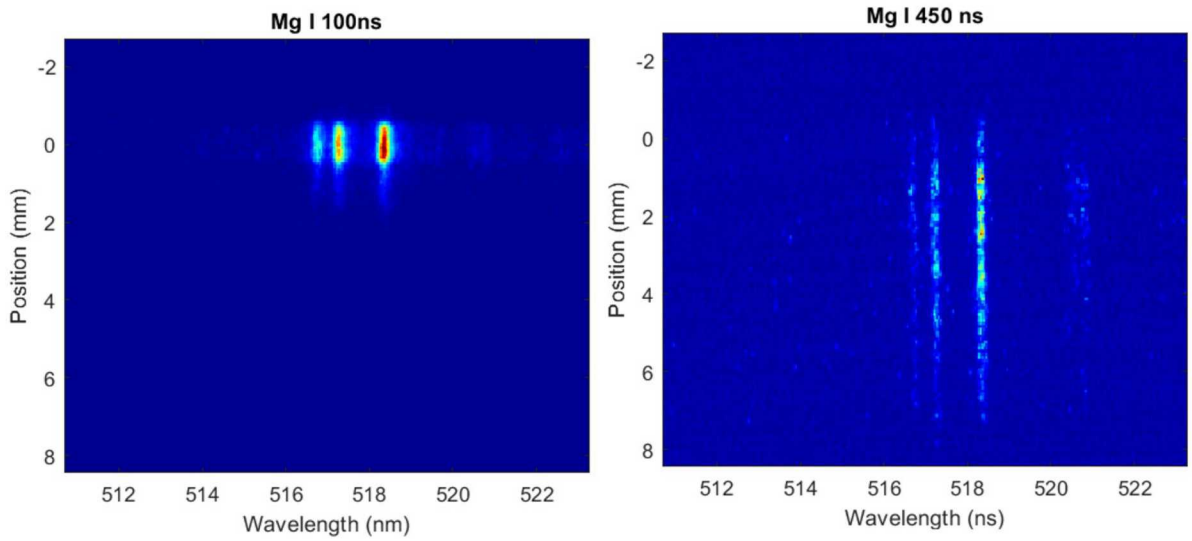

Figure 3-13. Calibrated data at 100 ns and 450 ns after the laser pulse

The Mg I line widths are, for the most part, comparable to the instrument resolution for electron density estimates. Peak densities occur within 100 ns after the laser pulse. Mg II would likely be a better candidate for these measurements. From PrismSpect simulations the Mg II/Mg I line ratio is greater than 1 over about 1 eV and by 1.2 eV the Mg II line is three orders of magnitude brighter than Mg I.

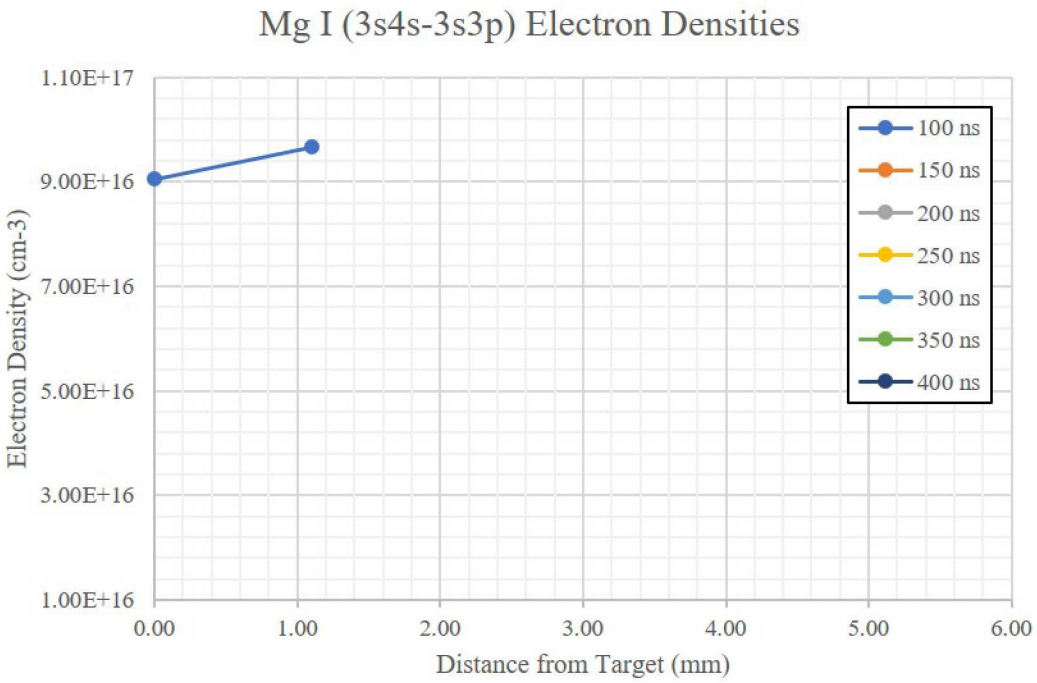

Figure 3-14. Estimated electron densities from the Mg I (3s4s-3s3p) line using Stark widths from [4].

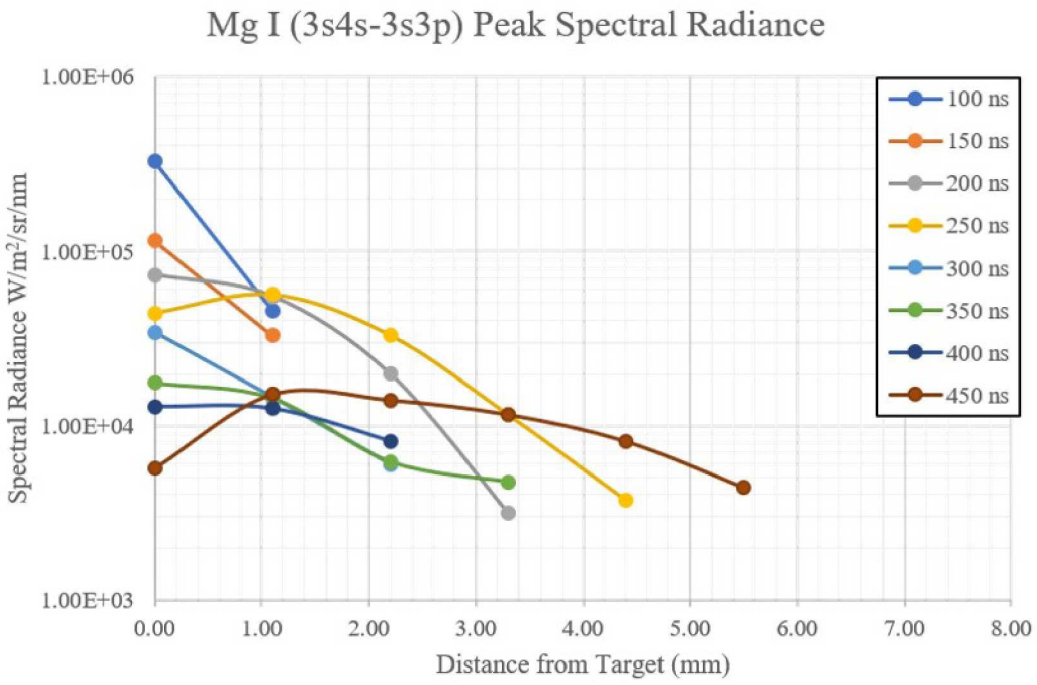

Figure 3-15. Peak Spectral Radiance

3.2.4. Cu I

The advantage of a metal dopant is primarily that a solid plug can be used and alignments can be verified by viewing the ablation plasma directly, rather than relying on the position sensing quad diodes. Although we have confirmed alignment can be easily achieved by using the quad diodes, and aligning the imaging fibers to the center of the beam line, the alignment of the imaging fibers to the plume is extremely sensitive. For a coated surface on Z, the alignment can not be directly verified without partially ablating away the dopant material. And so if the imaging fiber array were to be bumped, we would not know until after the shot.

Additionally, like Mg I, the Cu II lines appear at relatively cold temperatures, by about 1.4 eV the Cu I line at 520.7 nm is comparable to the Cu II lines between 490-500 nm, and so may be useful for electron temperature estimates.

The 3d4d-3d4p Cu I multiplet also has a larger Stark width (0.055 nm from [6]) than the other dopants that were tested. And so the lower limit for electron densities that could be measured at the 0.17 nm spectral resolution was about 1×10^{16} cm^{-3}.

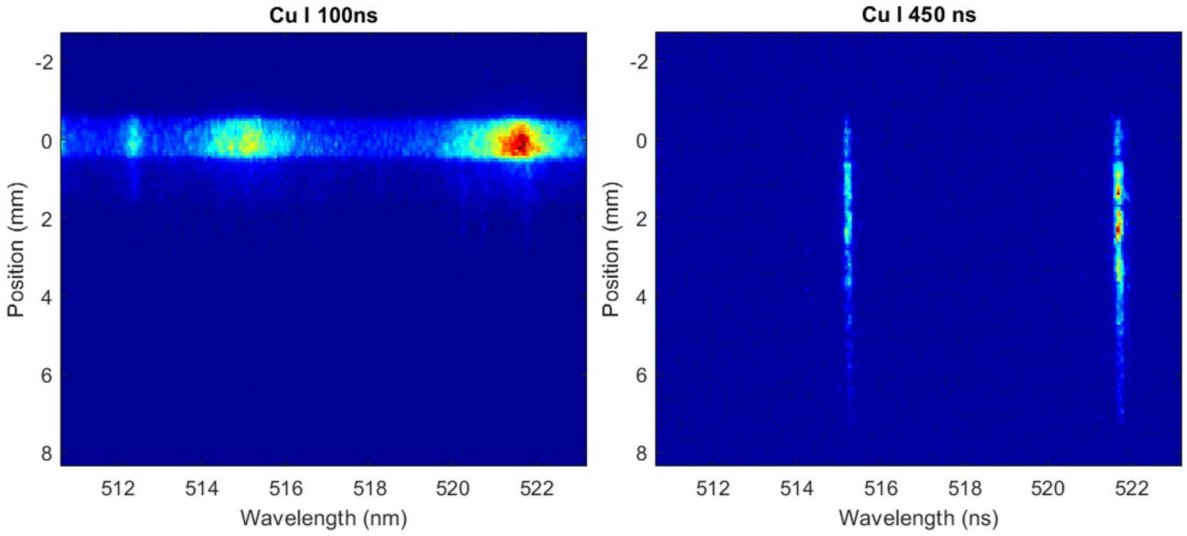

Figure 3-16. Calibrated data at 100 ns and 450 ns after the laser pulse

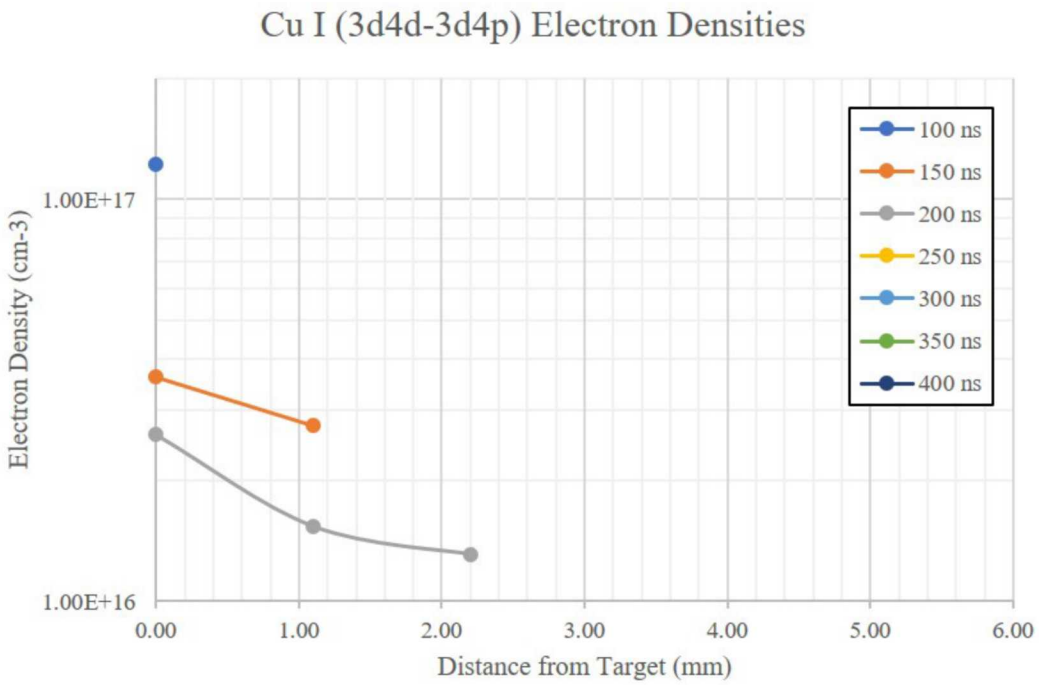

Figure 3-17. Estimated electron densities from the Cu I (3d4d-3d4p) line using Stark widths from [6].

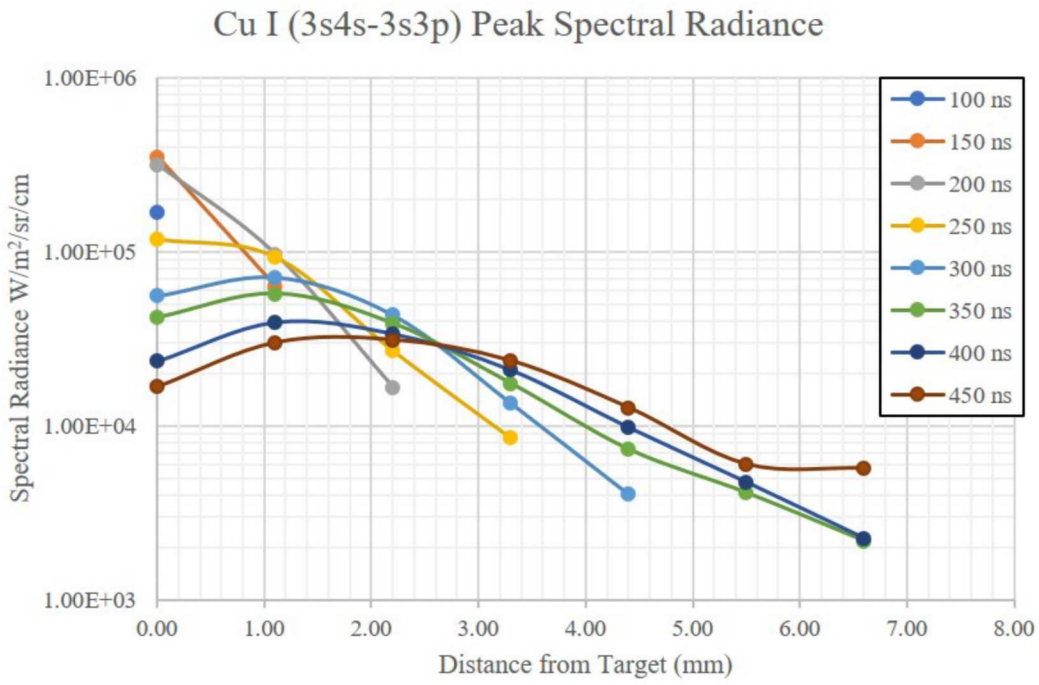

Figure 3-18. Peak Spectral Radiance

3.3. Spatial Filtering and Fiber Optic Delivery

Due to the short timescale of the project, only a small effort was invested in the optical beam train design and evaluation of laser parameters for generating adequate plasmas. The spectroscopic data described here show electron densities 1×10^{16}-4×10^{16} cm^{-3} or less at the lower bound. A more optimized beam train would produce a higher densities or similar densities at lower laser fluences. The following is a detailed discussion regarding the performance of the systems as used for this LDRD and suggested improvements for a second generation device.

3.3.1. Laser Quality

The laser system used in this LDRD, the Tempest 10 Hz, is a 5–10 ns 200 mJ class laser which has an inherently distorted beam due to the high-gain short length cavity. As such, the M^2 value of the beam is somewhere between 2 and 4 depending on factors such as flash lamp intensity, Q-switch timing, and cleanliness of external optics. With such a high M^2 value, the diffraction limited spot size is 2-4x larger resulting in a reduction in the peak fluence at the beam waist by a factor of 4 to 16. The diffraction limited spot size is given by $4M^2 f\lambda/(\pi D)$, where f is the focal length, λ is the laser wavelength, and D is the diameter of the laser beam.

Typically, a poor quality beam such as this would be remedied by spatially filtering the beam. In the case of a high-energy pulsed lasers, this spatial filtering is typically done in vacuum to prevent laser induced plasma generation in unconditioned air which occurs at a peak irradiance of 2×10^{11}–4×10^{11} $\mathrm{W\,cm}^{-2}$. for a 5-10 ns pulse. Since there was no readily available vacuum spatial filter, the authors opted to use a 200 um spatial filter at low enough laser energies (<10 mJ) to prevent breakdown in air. However, this still resulted in a poor quality beam as discussed in detail below. In a second generation device, it would be best to acquire a laser with a higher quality beam such as the Lumibird Viron which has an M^2 of 1.4 which would alleviate the need for any additional spatial filtering.

3.3.2. Fiber Delivery

One method for delivering high-energy pseudo single-mode pulses was established in previous work by S. Simpson et al. In this previous work, 15 mJ with t(FWHM)= 5 ns at 1064 nm could be propagated at distances of 1 m or further while maintaining an output M^2 of 1.4. The estimated peak irradiance at the final focus of their system was greater than 1×10^{12}–1×10^{13} $\mathrm{W\,cm}^{-2}$.

Albeit this appears an elegant solution, there are several issues with using such a system for future experiments on the Z-Machine. The advantage of using a fiber delivered technique is its insensitivity to motion induced misalignment since the beam is in a waveguide. However, the use of an alignment system, such as the one demonstrated on this LDRD, allows for remote realignment of the system within a few short minutes. The use of a novel fiber delivery system also requires a much more complex optical train for safely launching into the fiber. The system requires vacuum based spatial filtering, mode matching, and heightened cleanliness to prevent fiber damage when coupling and decoupling the pulse. Lastly, the cost of the proprietary fiber is

$1k per foot which would result in $20k per shot (due to fiber damage) on Z just for the fiber alone.

For the reasons mentioned above, a much simpler system using a single high quality laser with no spatial filtering and employing an automated alignment system would allow for delivering <30 mJ into a 10-15 um spot at final focus with a minimal optical train and avoiding the complexity of fiber coupling.

3.3.3. Spatially Filtered Measurements

The beam is focused down to about a 0.7 mm diameter spot size, unfiltered, and a 0.4 mm diameter after spatial filtering at 10% of peak intensity. The filtered measurement was taken using a 200um spatial filter in air, which limited the beam input energy. As shown in Figure 3-19 spatial filtering tightens the beam focus as well as improves the beam quality. Laser fluence was not be estimated for the purposes of this EE LDRD from the burn paper, as the beam is neither flat nor gaussian in the unfiltered case, and hot spots were present. As a result, all plots of laser energy in this report are measurements specific to the particular laser, and cannot be cross compared to other lasers with higher beam quality. A more gaussian input beam with a different laser or vacuum spatial filtering with a smaller pinhole would likely improve estimates of the fluence and reduce hot spots.

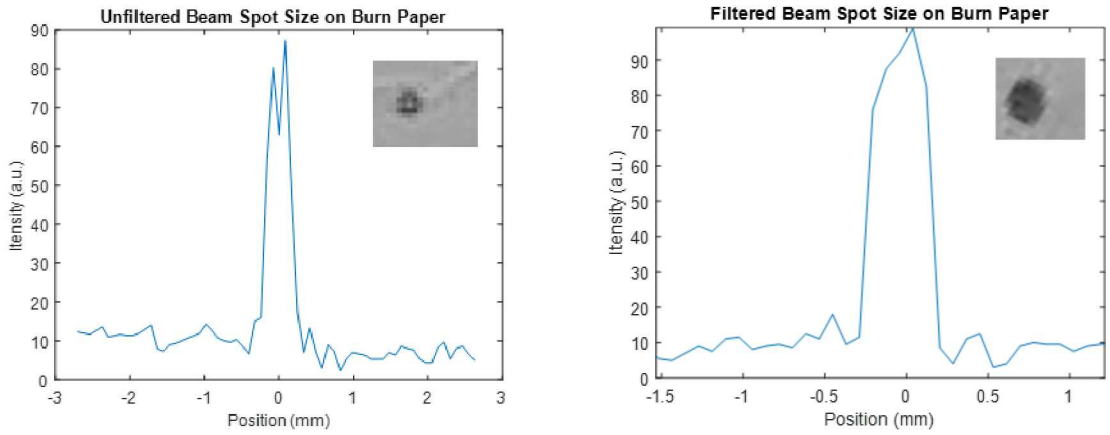

(a) Unfiltered **(b)** Filtered

Figure 3-19. Unfiltered and filtered beam profiles. Spatial filtering removes the central hole in the unfiltered beam.

The output of a fiber coupled laser system would have a high quality beam with an M^2 of 1.4, and so irradiances at the focus would likely be higher than in the unfocused case, even at lower input laser energy. And so to test whether much lower laser energy coupled through a fiber can produce sufficiently intense spectral lines from the doped target, we spatially filtered the initial beam with a a 200 um spatial filter in air. While a Gaussian beam was not achieved using the spatial filter, the beam quality was improved. In order to launch this beam into a fiber, however, we would need

to filter the beam under vacuum with a smaller diameter spatial filter, increasing complexity and alignment times.

The intensity ratio of Li I (670.8 nm) between the unfiltered and filtered beam focused on a LiF coated stainless disk are plotted in Figure 3-20. The unfiltered beam had a laser energy of about 105 uJ, while the filtered beam had an energy of 9.8 uJ at the target.

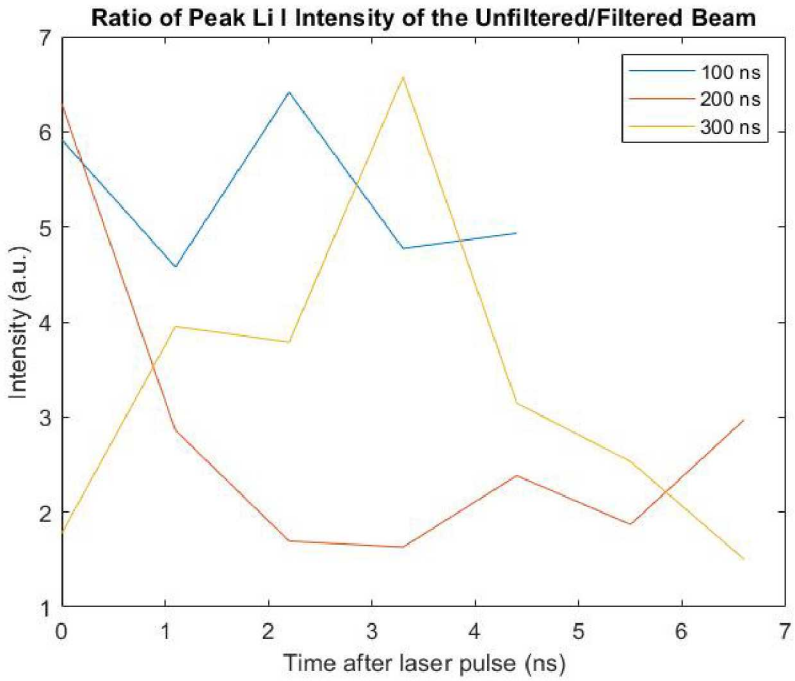

Figure 3-20. The unfiltered beam produces a Li plasma with a peak radiance from the 1s2p-1s2s line that varies from about twice as high as the filtered plasma to 6 times as high.

While the unfiltered beam at 105 uJ still produced more intense Li I lines, the filtered case with 10x less energy did produce measurable line emission. 10 uJ through a fiber, would have an even tighter spot size at the target, resulting in higher fluence. But while we may be able produce sufficient line intensity by delivering the laser energy through a fiber, the alignment process would be much more time consuming than delivering the energy through a closed beam path. The beam would have to be aligned through a spatial filter in vacuum and any minor bumps could prevent the beam energy from reaching the target. Additionally, the closed beam line is much more flexible in the densities we can produce on the target. Using a laser with a higher quality output beam would also improve the delivered energy density without sensitive alignments through vacuum spatial filters.

3.4. Uncertainties

Detailed error analysis has not been completed for this EE LDRD. Known uncertainties include small variations in the ratio of counts/intensity due to the ICCD and variations in the position of

the array relative to the beam axis and target surface. Measurements parallel to the ablation surface should also be taken to understand the effect that misalignment of the imaging fiber array to the laser beam axis has on the density and therefore the signal strength. Qualitatively, moving the fiber array by about 1 mm off the beam axis resulted in almost no signal. Errors in the absolute calibration should also be accounted. Absolute intensity uncertainties on Z, with a similar calibration process are currently estimated to be about +/-15%, but a more thorough error estimate is in progress.

The density is estimated assuming a temperature of about 2 eV from the low resolution measurements (which did rely on an optically thin assumption). However, the temperature does vary as a function of time and distance from the ablation surface, and the Stark widths vary with temperature. In the case of Li I for instance, widths tabulated in [2], suggest that between 0.8 eV and 3.4 eV the variation in the width causes about a 10% change in the estimated electron density.

4. CONCLUSIONS

The eventual goal of these measurements is to field an active dopant diagnostic on the Z-machine, which would yield insight into field strengths within power flow regions and near the various loads. Here we have demonstrated we can achieve spectral radiances above 1×10^5 $\mathrm{W\,sr^{-1}\,nm^{-1}\,m^{-2}}$, which should be sufficient for SVS on Z to measure with typically fielded settings (150 g/mm, 100um diameter fiber, 200 ns sweep speed, 0.5 inch collecting lens). But this radiance is at the upper limit of what we have produced with the laser ablated plasma. Increasing the laser fluence would increase the line intensity, but also the electron density. A higher density plasma has a greater potential to affect power flow and increase shielding of external fields, and so we suggest improving the current capabilities of visible spectroscopy on Z to reach these lower density regimes.

By improving the efficiency of SVS by an order of magnitude so that we can measure 1×10^4 $\mathrm{W\,sr^{-1}\,nm^{-1}\,m^{-2}}$, we would reach much lower densities (1×10^{16} $\mathrm{cm^{-3}}$). Not only would this limit shielding of the field strengths, but it would also provide measurements up to a few millimeters from the surface, in regions where the line shapes are likely not dominated by Stark broadening. Improving the efficiency substantially would also enable higher resolution measurements, leading to more accurate estimates of the E and B-fields, as well as electron densities not due to the initial laser ablation pulse.

Switching the streak camera for a gated ICCD camera would trade time resolution for spatial resolution, but the gated camera would be much more efficient. Using 200 um fibers rather than 100 um fibers would also increase the collected light by a factor of 4 (if we also increase the spectrometer slit or demagnify the light at the input of the spectrometer). The fiber runs to SVS are also very long, and approximately 60-70 percent of the light is lost in the transmission. These runs could potentially be shortened, if necessary, by placing a smaller spectrometer and ICCD camera in one of the Z boats.

We also tested the remote alignment methods that would need to be implemented on Z. Using two quad diodes we were able to accurately center and align the beam. The system is designed to be

modular and enclosed. All open beam alignments can take place in a laser controlled area. The system can then be taken apart and reassembled in the Z boat. Final alignments should not take more than a few minutes, and can be done with the laser and beam fully enclosed.

Most of these measurements were taken on coated 304 SS disks. However, it may be better to use a solid material for alignment checks. By using a solid material, a pre-shot spectrum could be taken, in the absence of any perturbations due to the current pulse, and alignments could also be checked. This could not be done with a coated surface, because the laser pulse ablates away much of the dopant material.

In conclusion, the active dopant technique looks promising. Strong emission lines at low densities can be measured. Perturbations to these lines should effect the line shape much more clearly then the Stark dominated spectra we have measured when viewing the power flow surface directly.

Future work, prior to fielding this on Z, will include testing the diagnostic on Mykonos primarily to investigate the effect of introducing a 1e16-1e17/cc plasma within a power flow region. The same diagnostics will be used, along with B-dots to estimate the effect on current such a plasma will have and one of the Z SVS systems, which will enable us to test our efficiency improvements to SVS. Finally, the perturbations due to the Mykonos power pulse to the laser ablation line shapes will be analyzed.

REFERENCES

[1] JE Bailey, AB Filuk, AL Carlson, DJ Johnson, P Lake, EJ McGuire, TA Mehlhorn, TD Pointon, TJ Renk, WA Stygar, et al. Atomic emission spectroscopy in high electric fields. In AIP Conference Proceedings, volume 381, pages 245–258. AIP, 1996.

[2] Milan S Dimitrijevic and Sylvie Sahal-Bréchot. Stark broadening of Li II spectral lines. Physica Scripta, 54(1):50, 1996.

[3] MS Dimitrijevic and S Sahal-Bréchot. Tables for Na I lines stark broadening parameters. Bull. Obs. As1ron Belgrade N, 142:59–77, 1990.

[4] MS Dimitrijevic and Sylvie Sahal-Bréchot. Stark broadening parameter tables for Mg I lines of interest for solar and stellar spectra research. i. Bulletin Astronomique de Belgrade, 149:31–84, 1994.

[5] Matthew R Gomez, Stephanie B Hansen, Kyle J Peterson, DE Bliss, AL Carlson, DC Lamppa, DG Schroen, and GA Rochau. Magnetic field measurements via visible spectroscopy on the z machine. Review of Scientific Instruments, 85(11):11E609, 2014.

[6] S. Sahal-Bréchot, M.S. Dimitrijević, and N. Moreau. Stark-b database. http://stark-b.obspm.fr, 2019.

APPENDIX A. SPECTRAL FITS AND DATA

A.1. Li I (1s2p-1s2s)

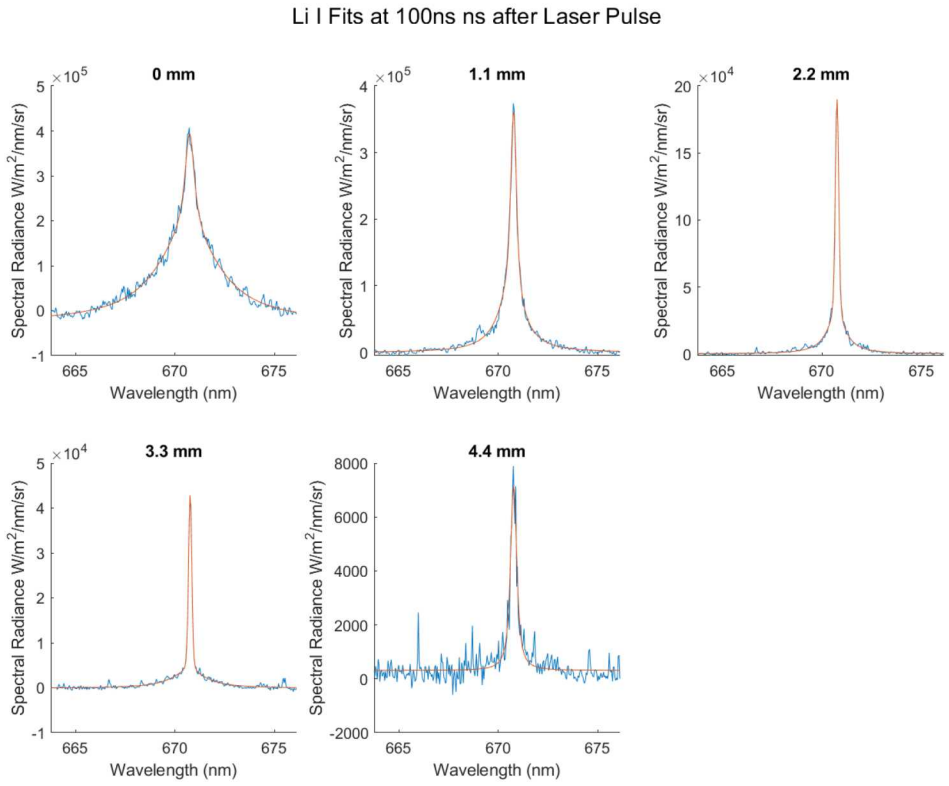

Figure A-1. Li I fits, 100 ns after laser pulse

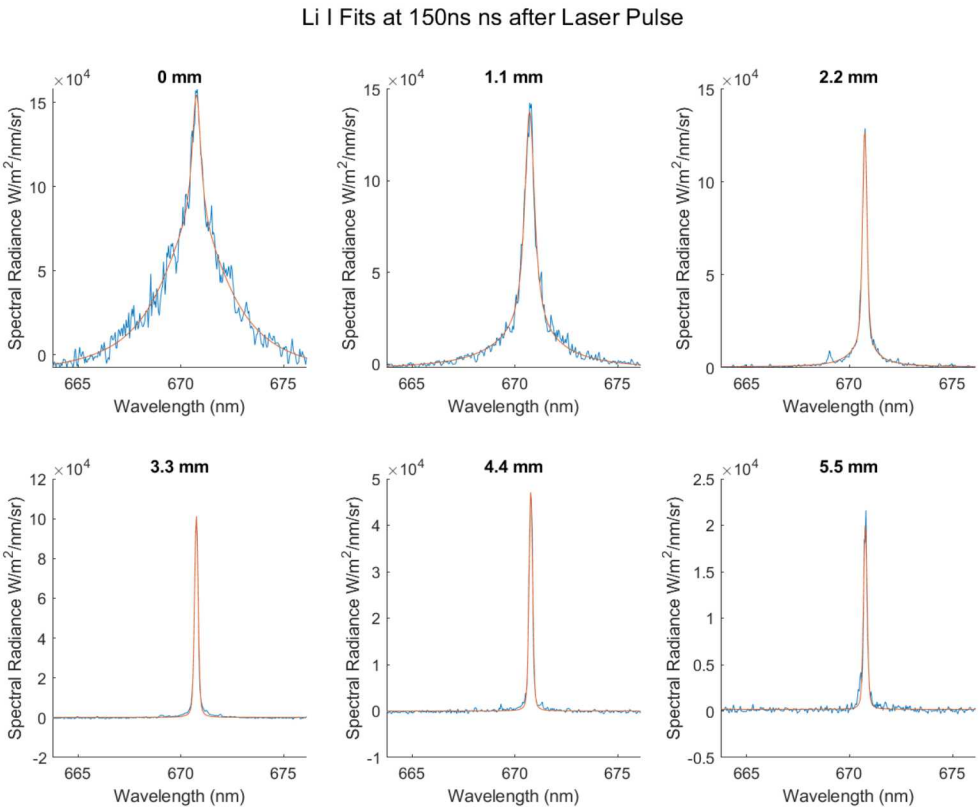

Figure A-2. Li I fits, 150 ns after laser pulse

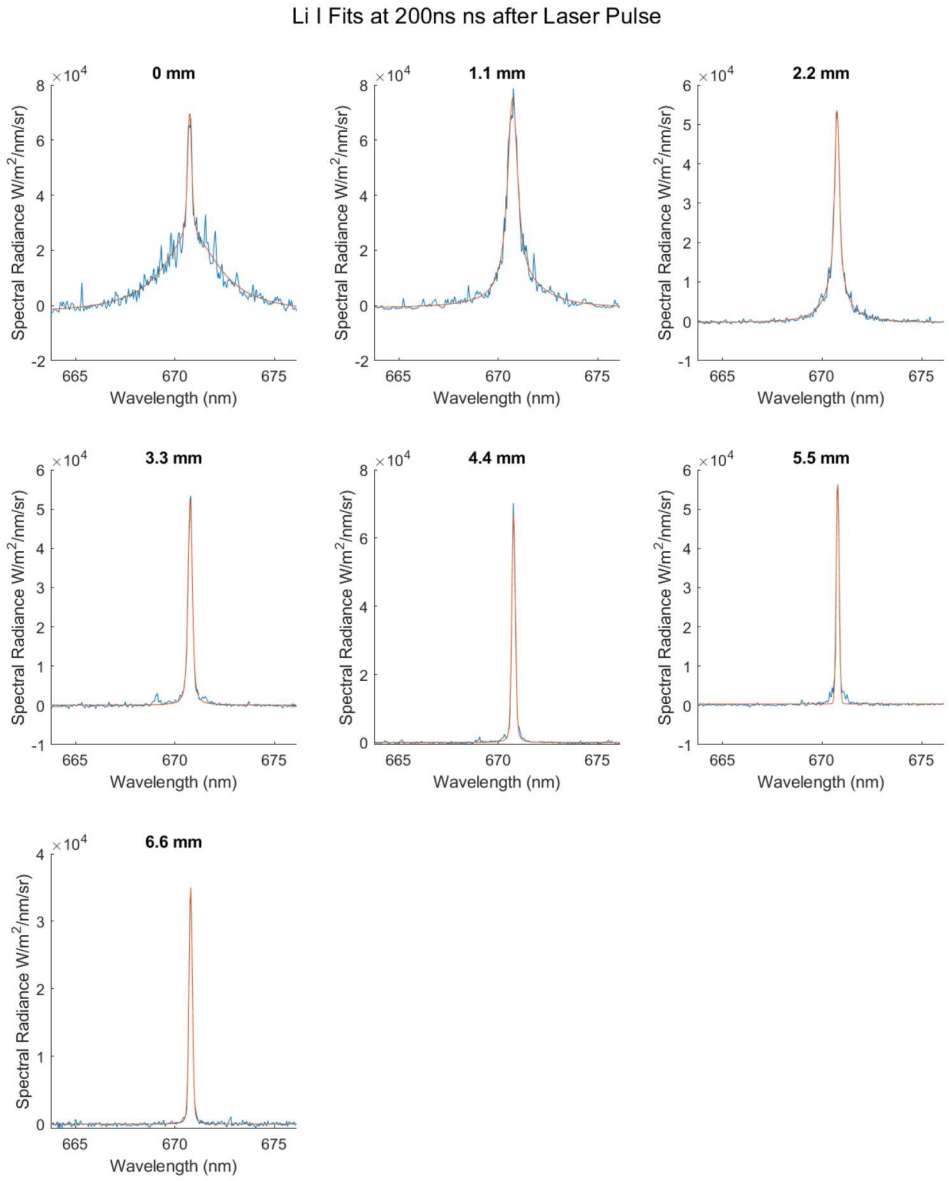

Figure A-3. Li I fits, 200 ns after laser pulse

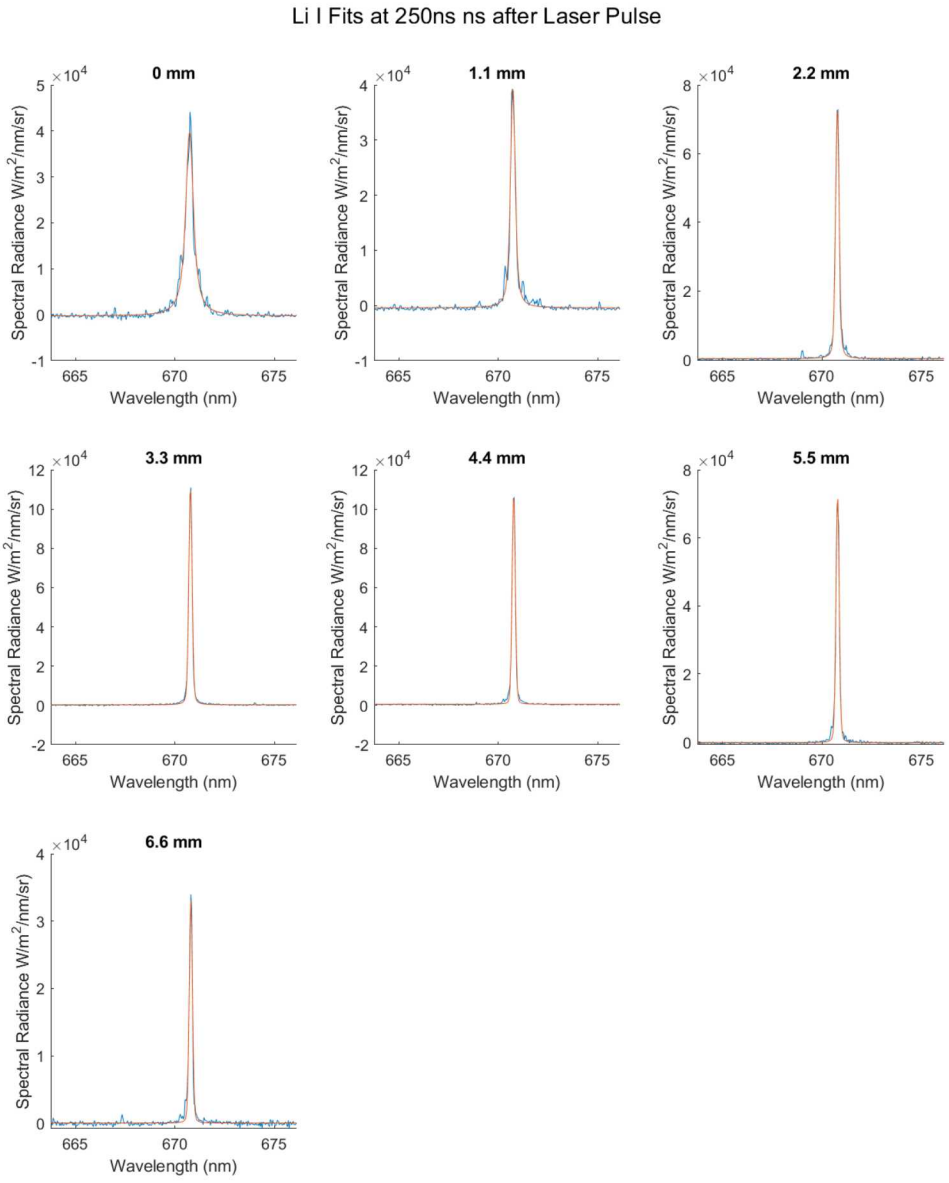

Figure A-4. Li I fits, 250 ns after laser pulse

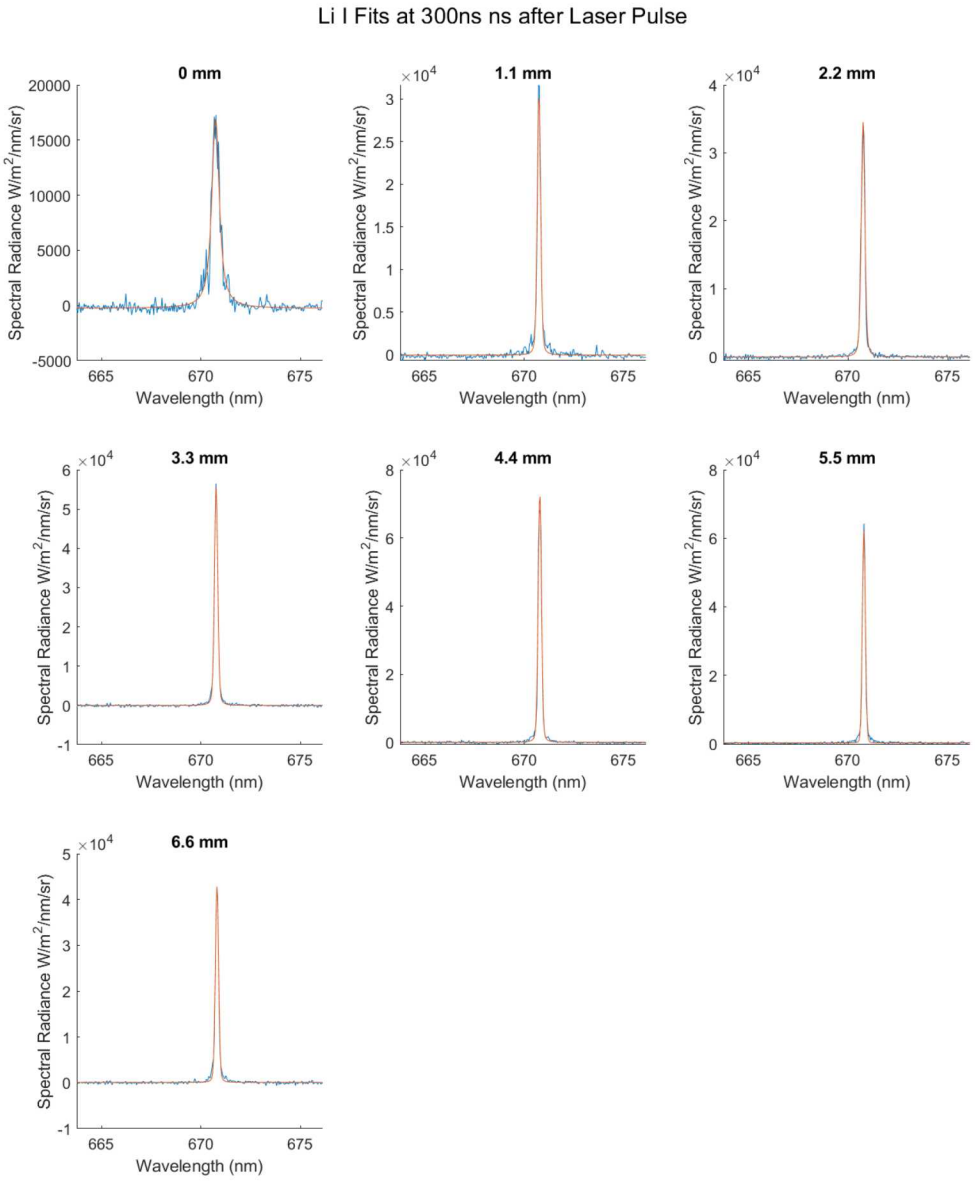

Figure A-5. Li I fits, 300 ns after laser pulse

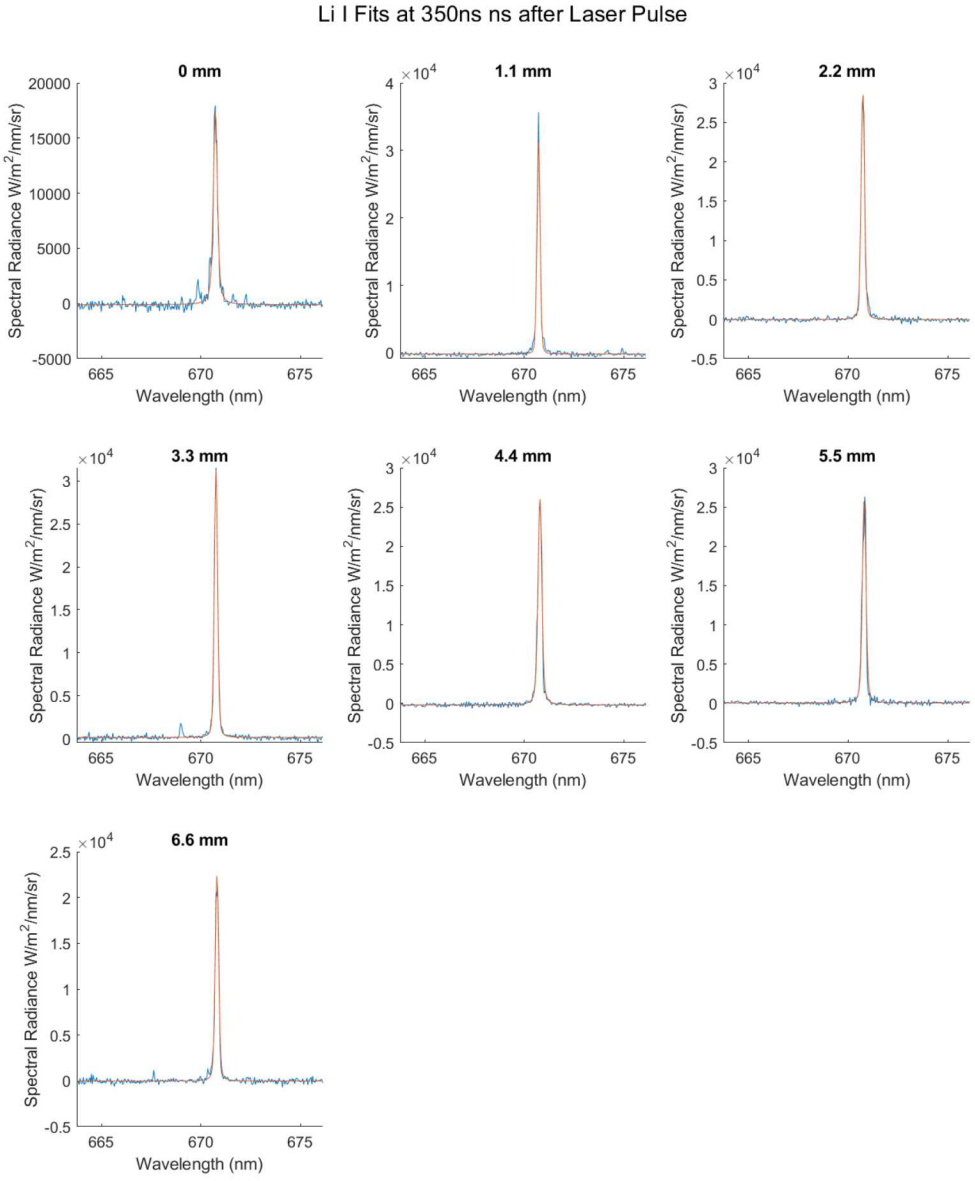

Figure A-6. Li I fits, 350 ns after laser pulse

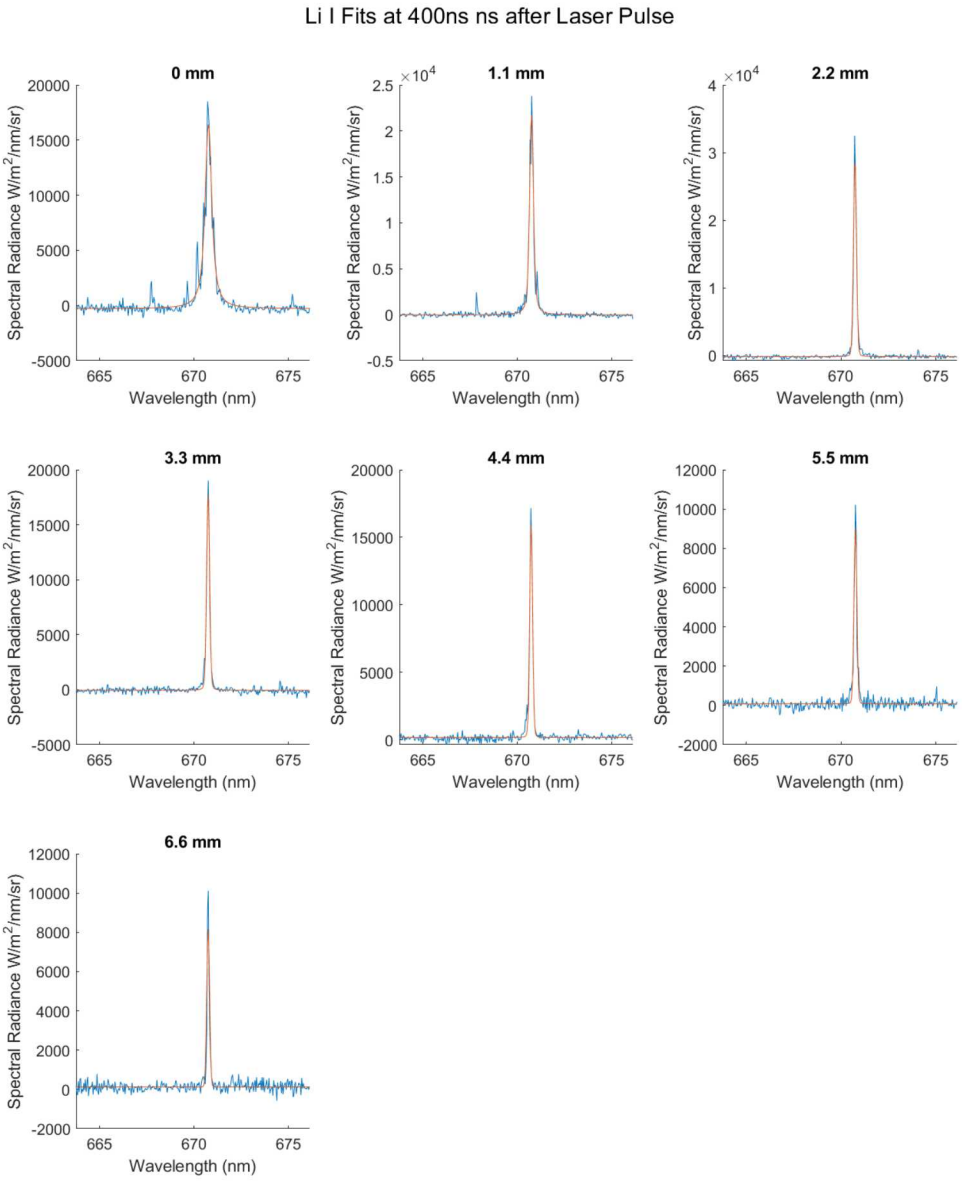

Figure A-7. Li I fits, 400 ns after laser pulse

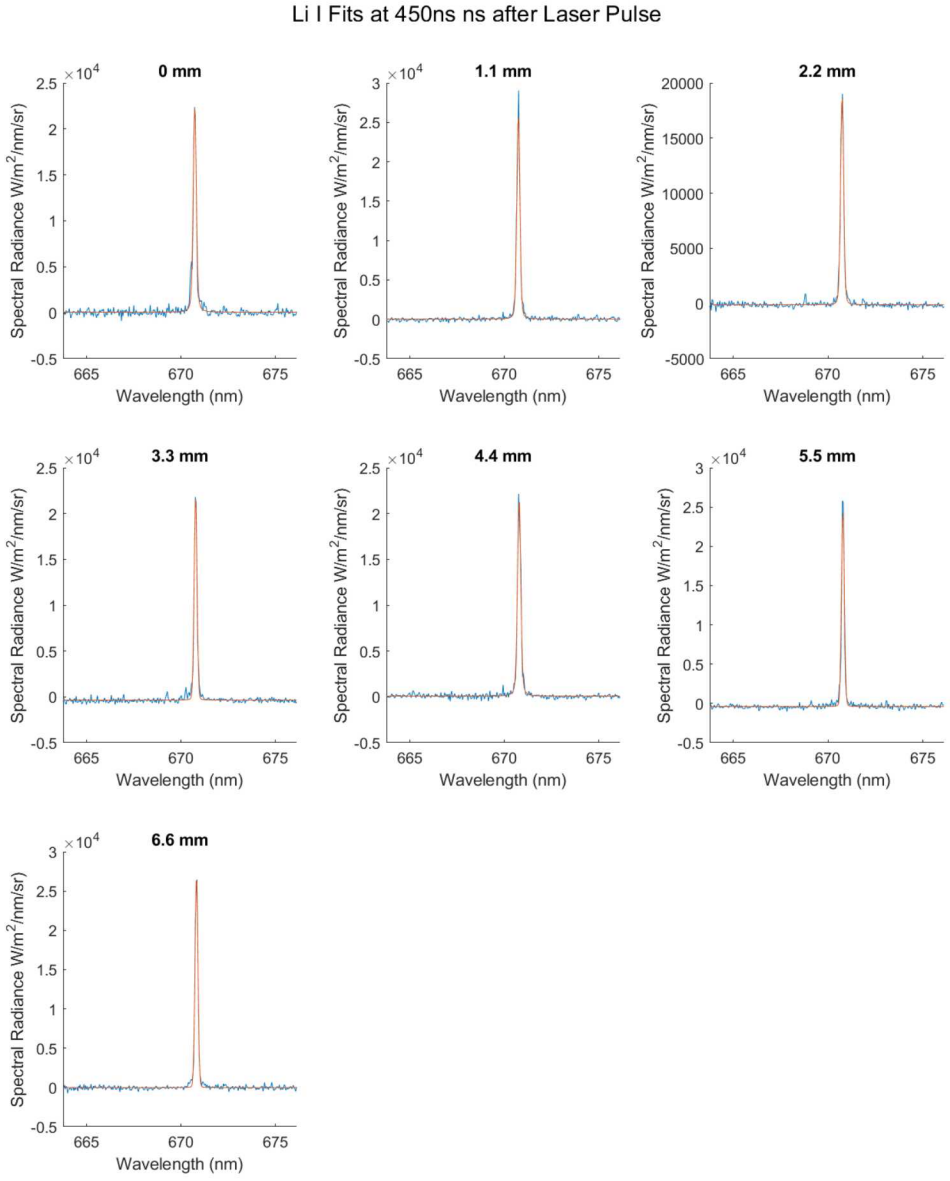

Figure A-8. Li I fits, 450 ns after laser pulse

Table A-1. Average Lorentzian line widths for Li I (670.8 nm), only widths greater than 0.03 nm are shown here. Gaussian widths are taken to be the instrument resolution of about 0.17 nm

	100 ns	150ns	200ns	250ns	300 ns	350 ns	400 ns	450 ns
0 mm	1.11E+00	1.16E+00	9.07E-01	1.39E-01	1.93E-01	6.61E-02	1.79E-01	
1.1 mm	4.55E-01	1.13E+00	8.98E-01	8.74E-02			5.76E-02	
2.2 mm	3.05E-01	4.32E-01	3.25E-01	3.15E-02	3.18E-02			
3.3 mm	5.35E-01	3.11E-02	6.60E-02					
4.4 mm								
5.5 mm		3.04E-02						
6.6 mm								

Table A-2. Estimated densities from line widths. Assumed Stark Width of 0.006 nm from [2]

	100 ns	150ns	200ns	250ns	300 ns	350 ns	400 ns	450 ns
0.00	1.83E+18	1.91E+18	1.50E+18	2.31E+17	3.20E+17	1.09E+17	2.97E+17	
1.10	7.53E+17	1.87E+18	1.49E+18	1.45E+17			9.54E+16	
2.20	5.05E+17	7.15E+17	5.38E+17	5.21E+16	5.26E+16			
3.30	8.86E+17	5.16E+16	1.09E+17					
4.40								
5.50		5.03E+16						
6.60								

Table A-3. Peak spectral radiance of Li I (670.8 ns)

	100 ns	150ns	200ns	250ns	300 ns	350 ns	400 ns	450 ns
0.00	4.20E+05	1.68E+05	7.34E+04	3.57E+04	1.72E+04	1.76E+04	1.67E+04	2.24E+04
1.10	3.65E+05	1.41E+05	7.71E+04	4.01E+04	3.09E+04	3.16E+04	2.18E+04	2.61E+04
2.20	1.90E+05	1.28E+05	5.41E+04	7.32E+04	3.46E+04	2.88E+04	2.92E+04	1.90E+04
3.30	4.31E+04	1.01E+05	5.28E+04	1.12E+05	5.57E+04	3.10E+04	1.79E+04	2.23E+04
4.40		4.77E+04	6.75E+04	1.08E+05	7.35E+04	2.64E+04	1.59E+04	2.15E+04
5.50		1.99E+04	5.63E+04	7.30E+04	6.21E+04	2.59E+04	8.95E+03	2.52E+04
6.60			3.52E+04	3.31E+04	4.29E+04	2.24E+04	8.09E+03	2.71E+04

A.2. Na I (2p3p-2p3s)

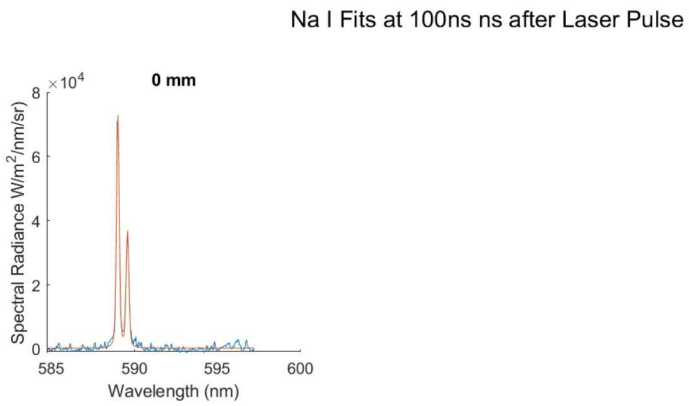

Figure A-9. Na I fits, 100 ns after laser pulse

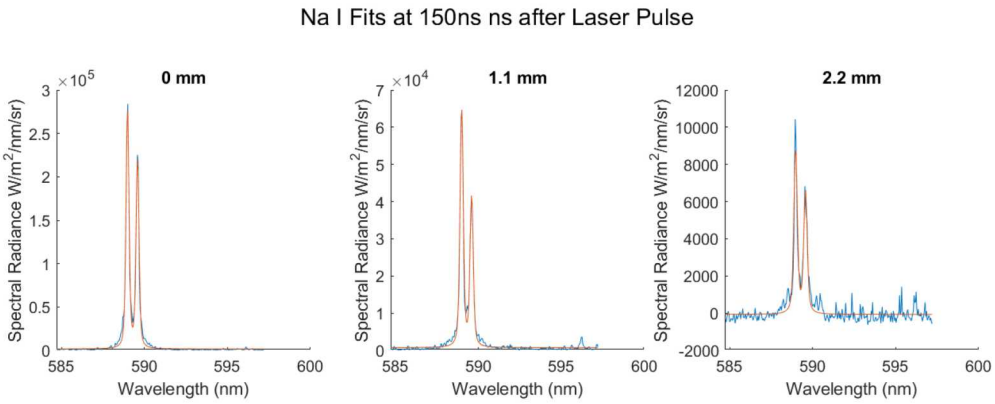

Figure A-10. Na I fits, 150 ns after laser pulse

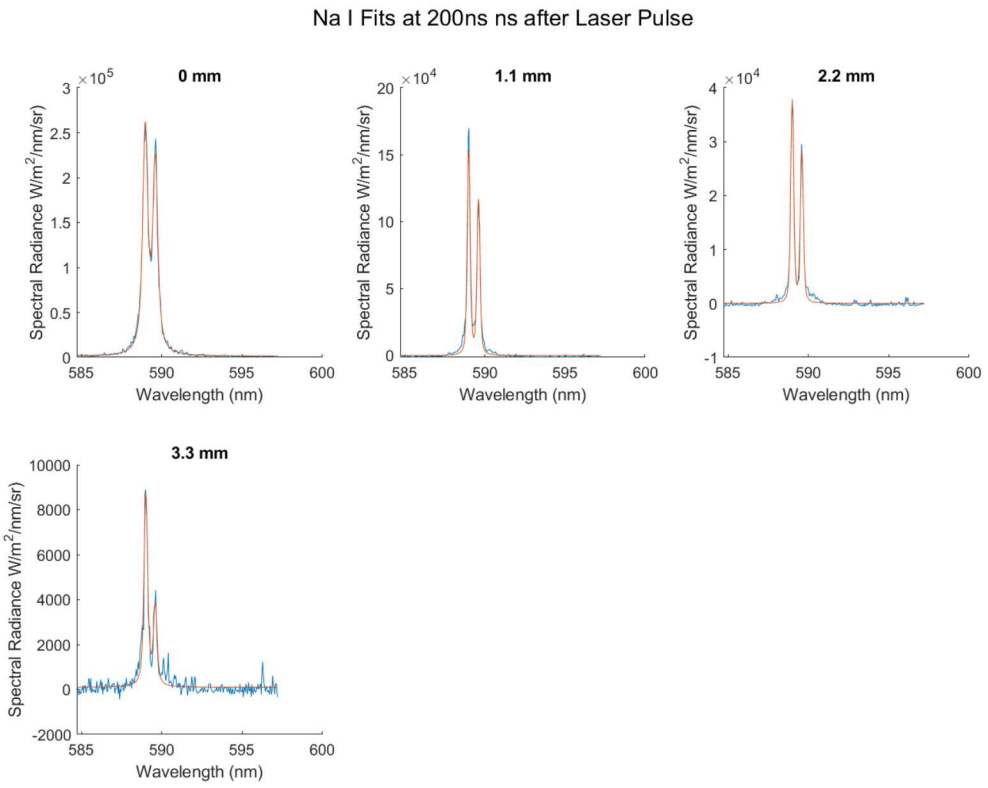

Figure A-11. Na I fits, 200 ns after laser pulse

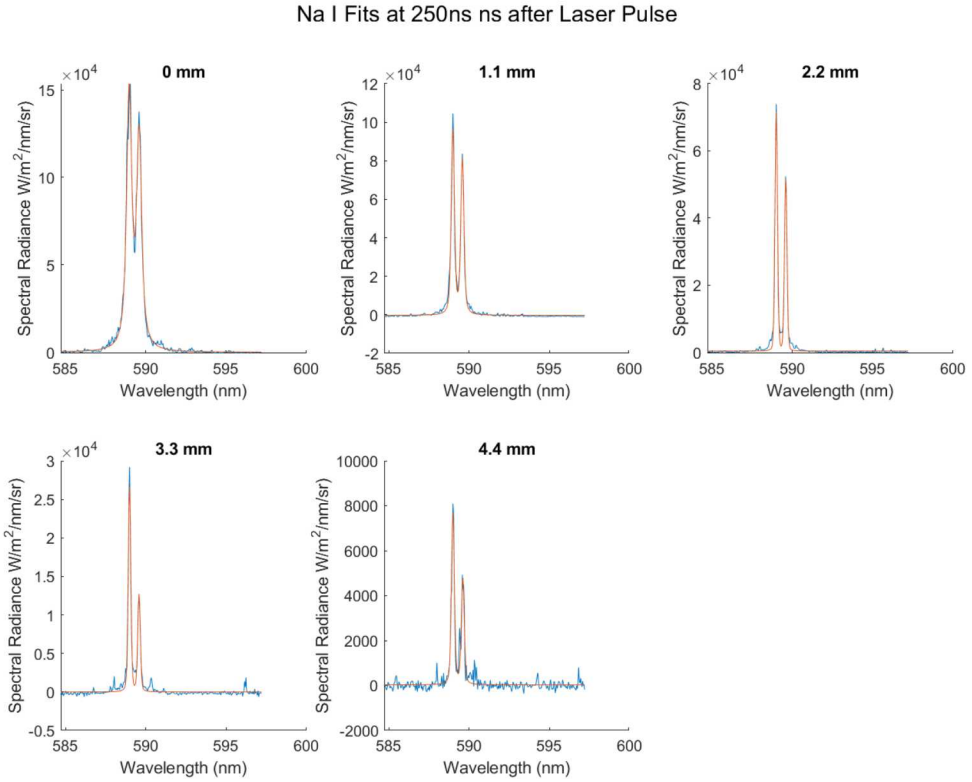

Figure A-12. Na I fits, 250 ns after laser pulse

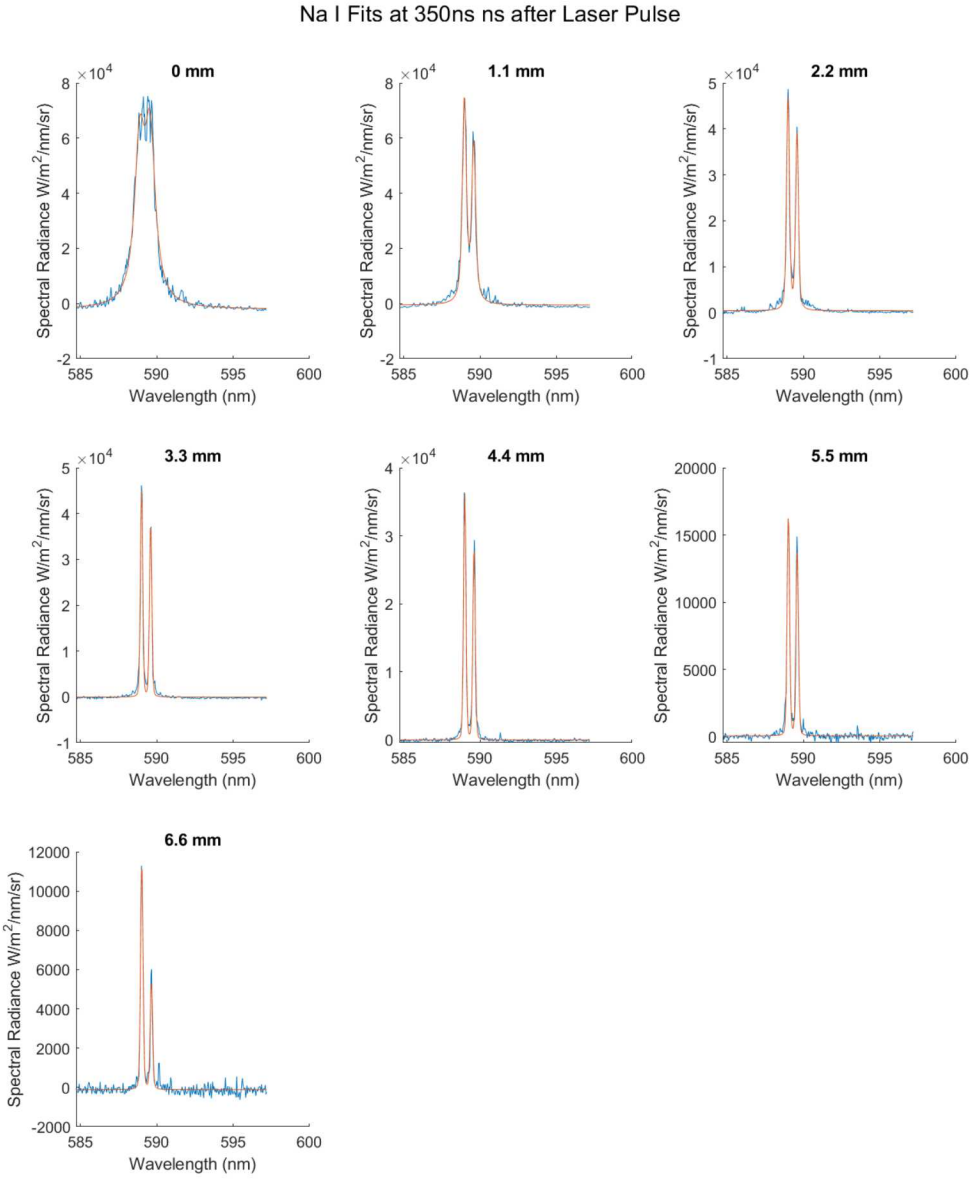

Figure A-13. Na I fits, 350 ns after laser pulse

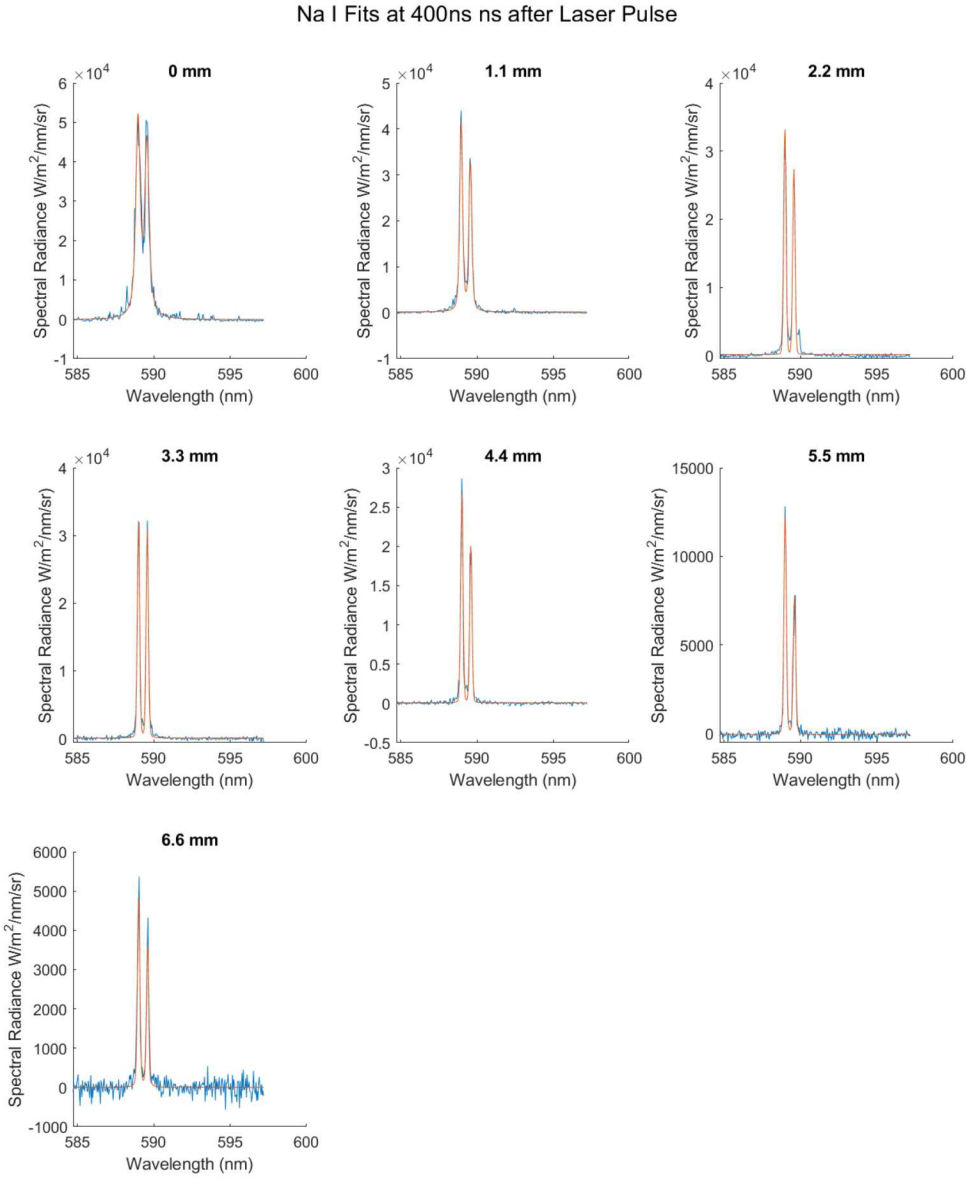

Figure A-14. Na I fits, 400 ns after laser pulse

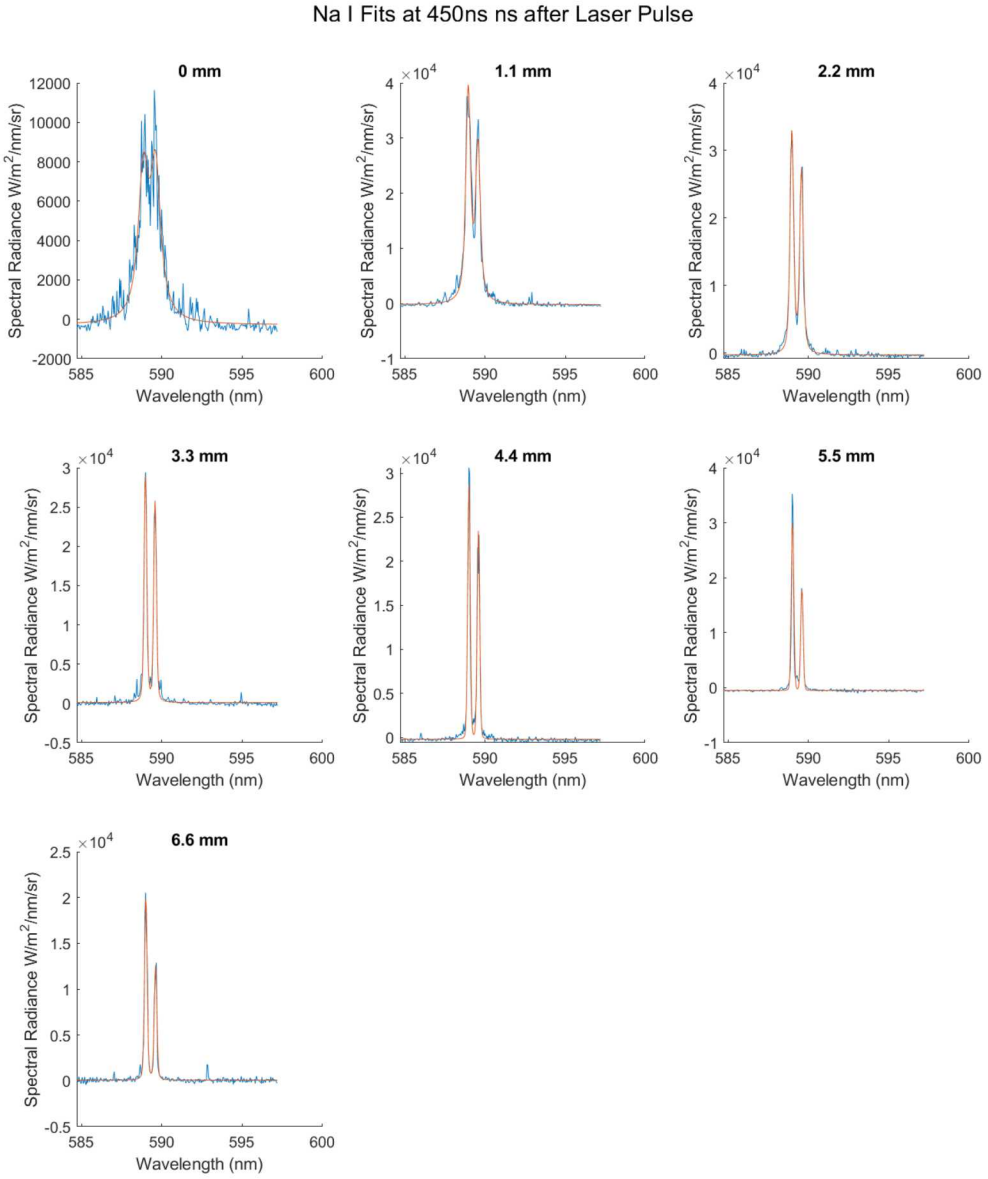

Figure A-15. Na I fits, 450 ns after laser pulse

Table A-4. Average Lorentzian line widths for Na I (2p3p-2p3s), only widths greater than 0.03 nm are shown here. Gaussian widths are taken to be the instrument resolution of about 0.17 nm

	100 ns	150ns	200ns	250ns	350 ns	400 ns	450 ns
0 mm	0.030	0.044	0.149	0.152	0.389	0.130	0.364
1.1 mm		0.051	0.042	0.051	0.106	0.048	0.133
2.2 mm		0.061	0.041	0.036	0.044		0.069
3.3 mm			0.083				
4.4 mm				0.036			
5.5 mm							
6.6 mm							

Table A-5. Estimated densities from line widths. Assumed Stark Width of 0.0064 nm from [3]

	100 ns	150ns	200ns	250ns	350 ns	400 ns	450 ns
0 mm	4.93E+16	7.31E+16	2.47E+17	2.51E+17	6.44E+17	2.14E+17	6.02E+17
1.1 mm		8.50E+16	7.02E+16	8.50E+16	1.76E+17	7.99E+16	2.21E+17
2.2 mm		1.01E+17	6.87E+16	5.99E+16	7.22E+16		1.15E+17
3.3 mm			1.38E+17				
4.4 mm				5.99E+16			
5.5 mm							
6.6 mm							

Table A-6. Peak spectral radiance of Na I (2p3p-2p3s)

	100 ns	150ns	200ns	250ns	350 ns	400 ns	450 ns
0 mm	7.24E+04	2.74E+05	2.49E+05	1.46E+05	5.50E+04	5.00E+04	7.29E+03
1.1 mm		6.38E+04	1.54E+05	9.59E+04	7.38E+04	4.11E+04	3.83E+04
2.2 mm		8.83E+03	3.76E+04	7.64E+03	4.62E+04	3.34E+04	3.30E+04
3.3 mm			8.57E+03	2.67E+04	4.51E+04	3.21E+04	2.89E+04
4.4 mm				7.64E+03	3.62E+04	2.66E+04	2.90E+04
5.5 mm					1.64E+04	1.23E+04	3.11E+04
6.6 mm					1.16E+04	4.87E+03	2.00E+04

A.3. Mg I (3s4s-3s3p)

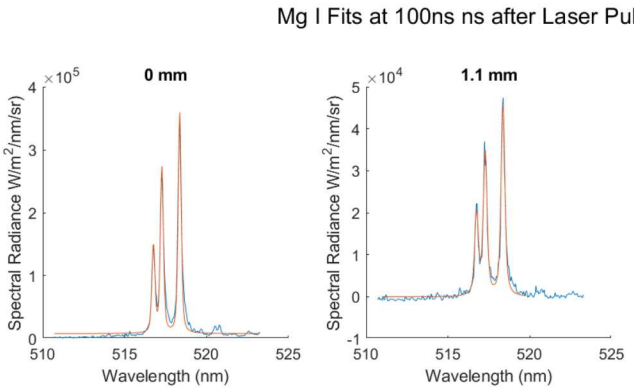

Figure A-16. Mg I fits, 100 ns after laser pulse

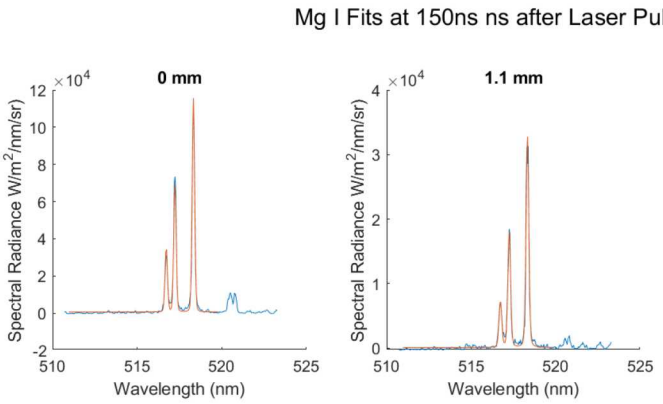

Figure A-17. Mg I fits, 150 ns after laser pulse

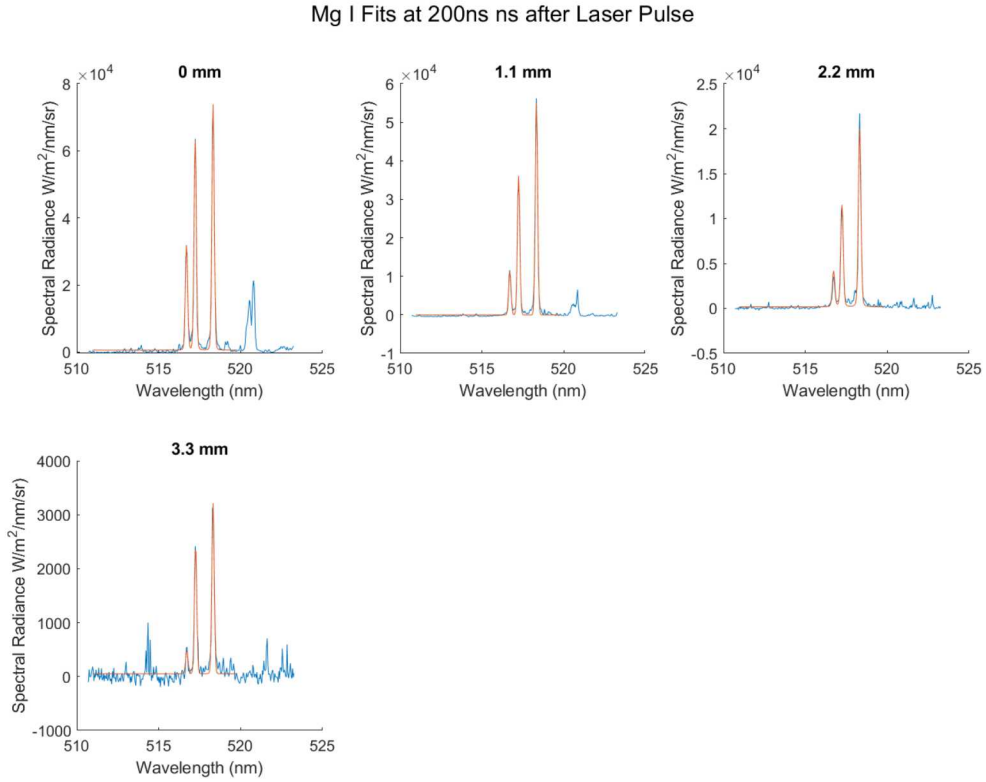

Figure A-18. Mg I fits, 200 ns after laser pulse

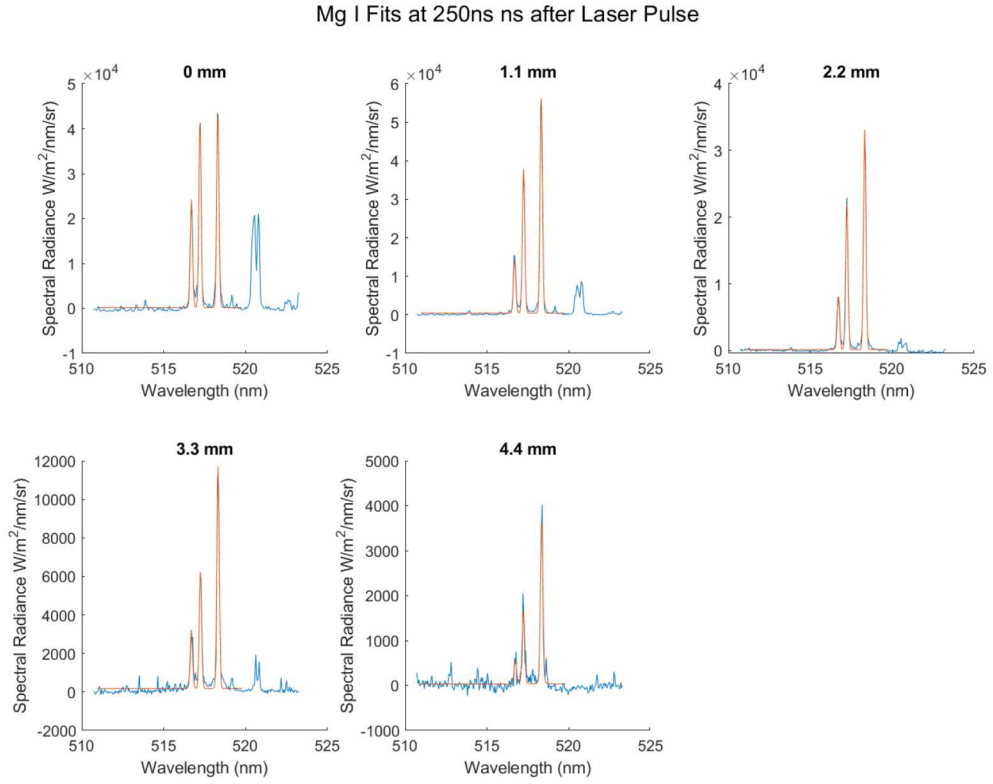

Figure A-19. Mg I fits, 250 ns after laser pulse

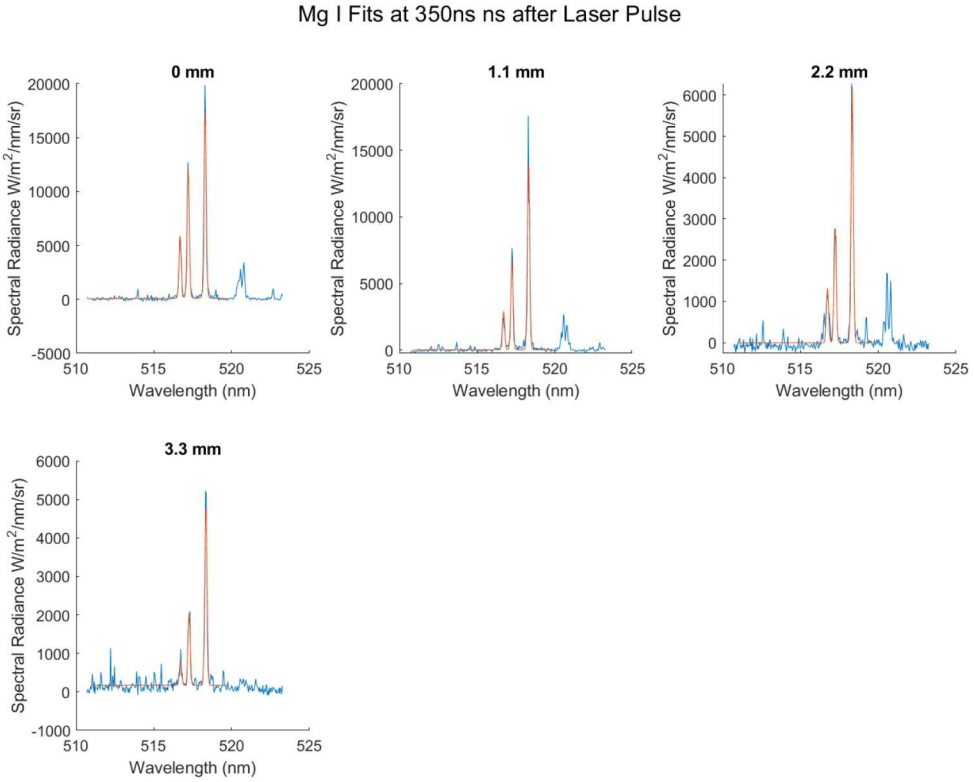

Figure A-20. Mg I fits, 350 ns after laser pulse

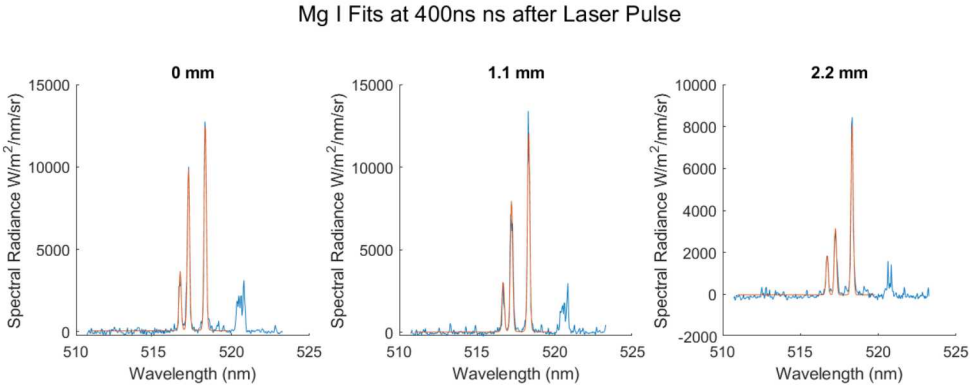

Figure A-21. Mg I fits, 400 ns after laser pulse

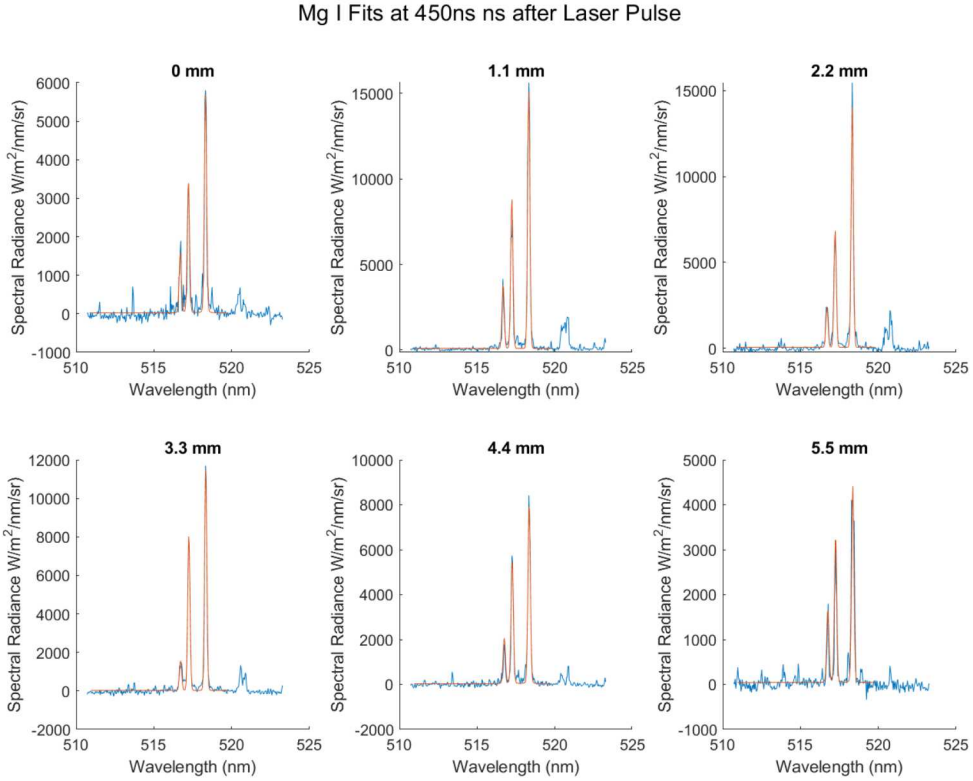

Figure A-22. Mg I fits, 450 ns after laser pulse

Table A-7. Average Lorentzian line widths for Mg I (3s4s-3s3p), only widths greater than 0.03 nm are shown here. Gaussian widths are taken to be the instrument resolution of about 0.17 nm

	100 ns	150ns	200ns	250ns	300 ns	350 ns	400 ns	450 ns
0 mm	7.69E-02							
1.1 mm	8.21E-02							
2.2 mm								
3.3 mm								
4.4 mm								
5.5 mm								
6.6 mm								

Table A-8. Estimated densities from line widths. Assumed Stark Width of 0.0085 nm at 1e16/cc from [4]

Table A-9. Add caption

	100 ns	150ns	200ns	250ns	300 ns	350 ns	400 ns	450 ns
0 mm	9.05E+16							
1.1 mm	9.66E+16							
2.2 mm								
3.3 mm								
4.4 mm								
5.5 mm								
6.6 mm								

Table A-10. Peak spectral radiance of Mg I (3s4s-3s3p)

Table A-11. Add caption

	100 ns	150ns	200ns	250ns	300 ns	350 ns	400 ns	450 ns
0 mm	3.29E+05	1.14E+05	7.33E+04	4.42E+04	3.44E+04	1.76E+04	1.29E+04	5.69E+03
1.1 mm	4.56E+04	3.29E+04	5.51E+04	5.63E+04	1.46E+04	1.44E+04	1.23E+04	1.51E+04
2.2 mm			1.99E+04	3.29E+04	6.03E+03	6.21E+03	8.16E+03	1.40E+04
3.3 mm			3.17E+03	1.15E+04		4.74E+03		1.16E+04
4.4 mm				3.70E+03				8.11E+03
5.5 mm								4.38E+03
6.6 mm								

A.4. Cu I (3d4d-3d4p)

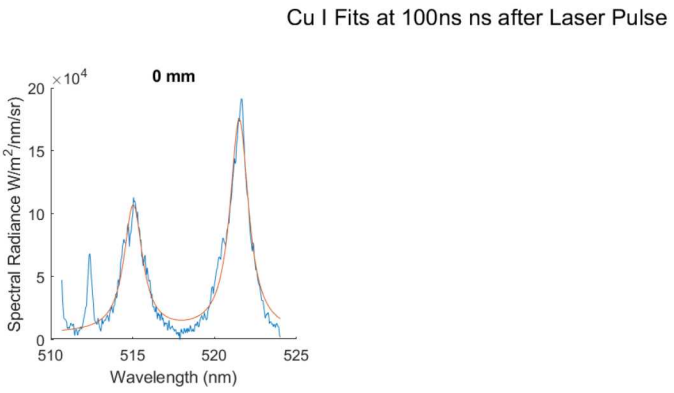

Figure A-23. Cu I fits, 100 ns after laser pulse

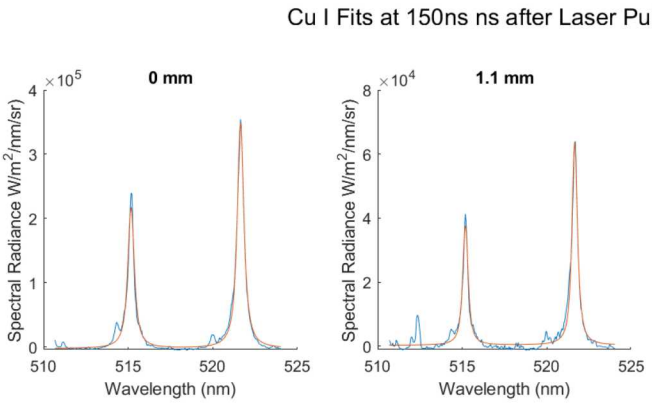

Figure A-24. Cu I fits, 150 ns after laser pulse

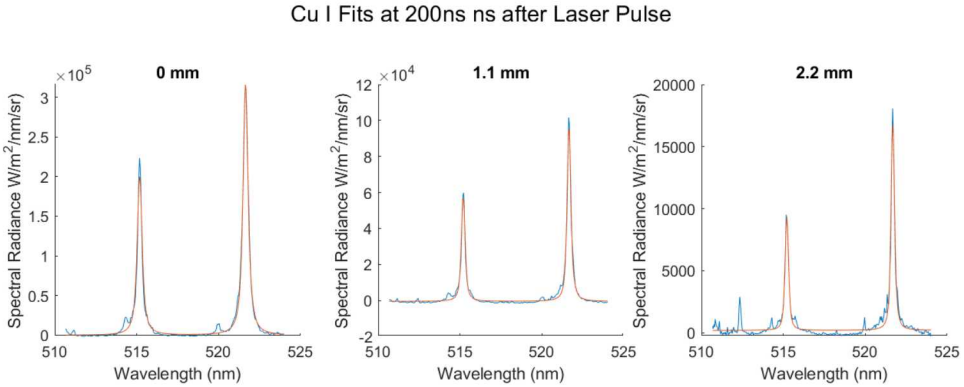

Figure A-25. Cu I fits, 200 ns after laser pulse

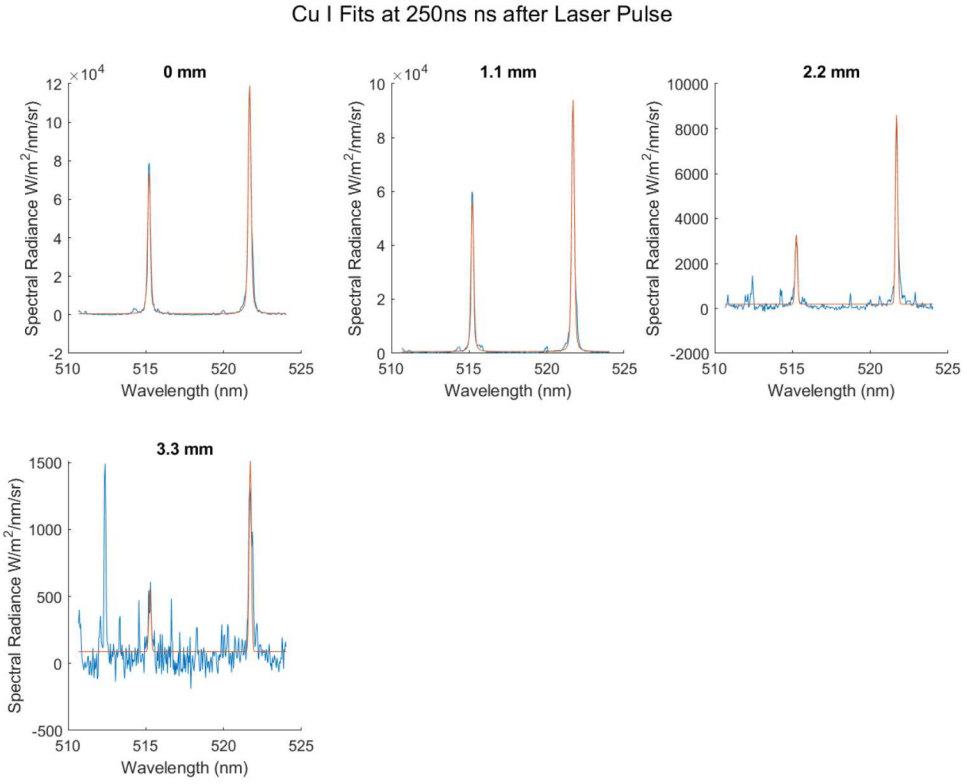

Figure A-26. Cu I fits, 250 ns after laser pulse

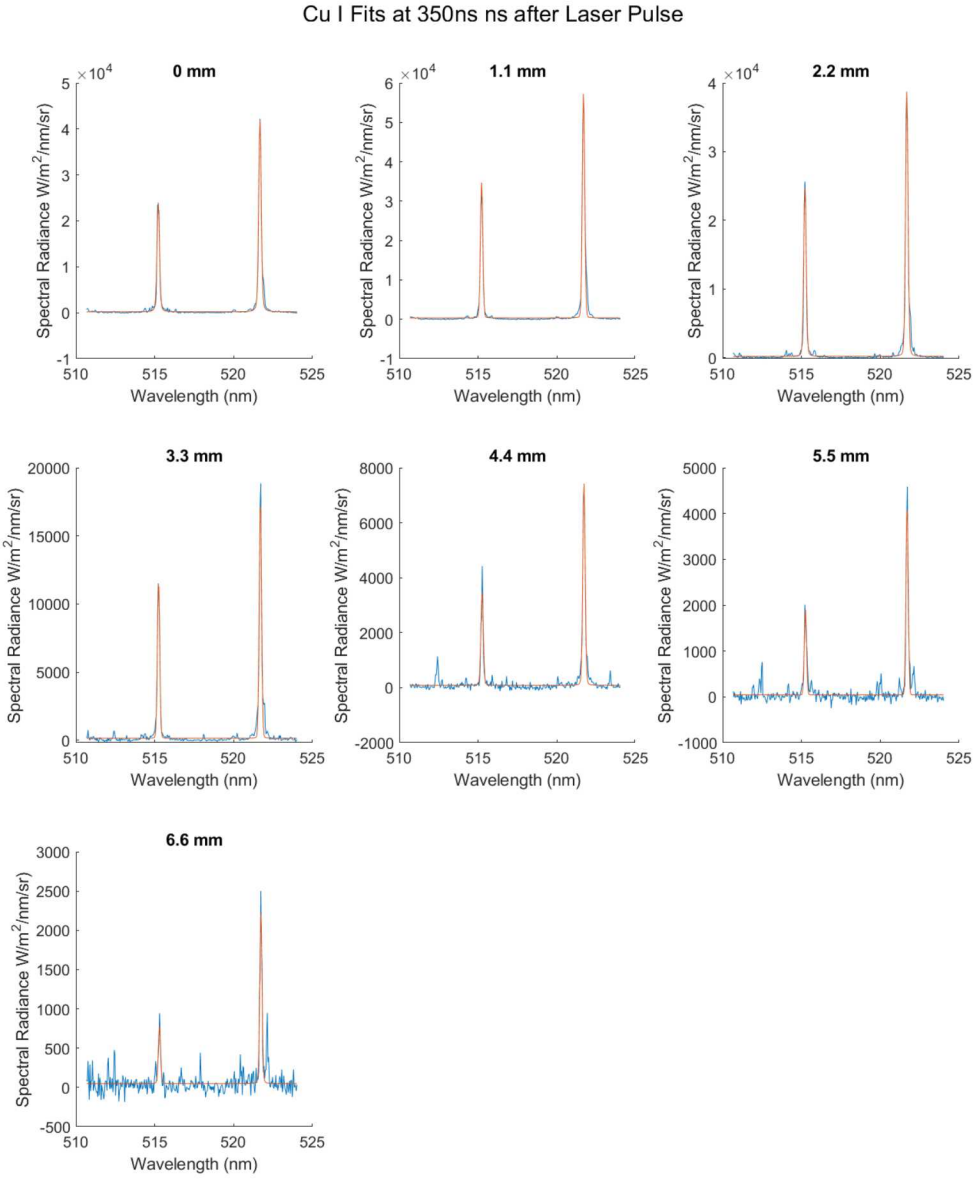

Figure A-27. Cu I fits, 350 ns after laser pulse

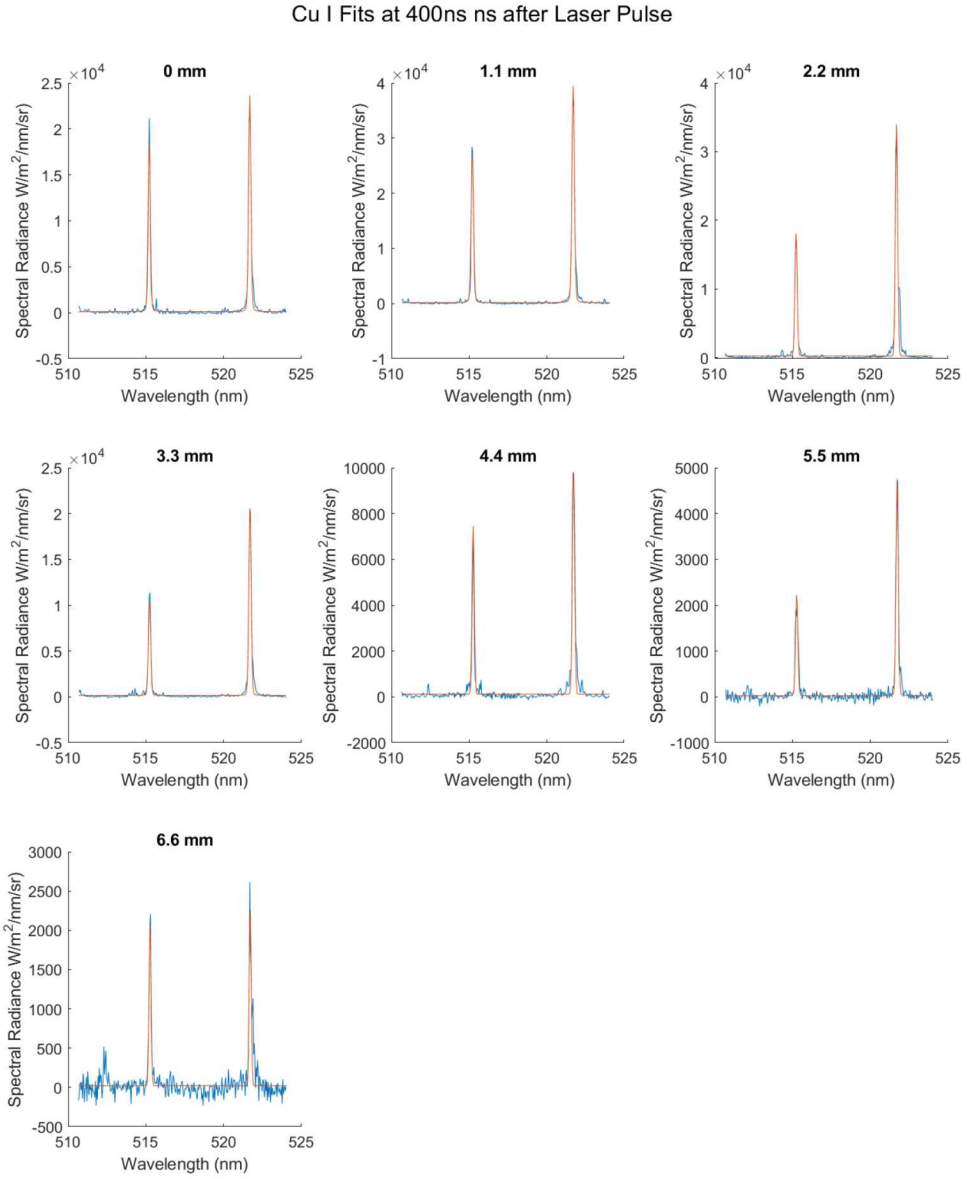

Figure A-28. Cu I fits, 400 ns after laser pulse

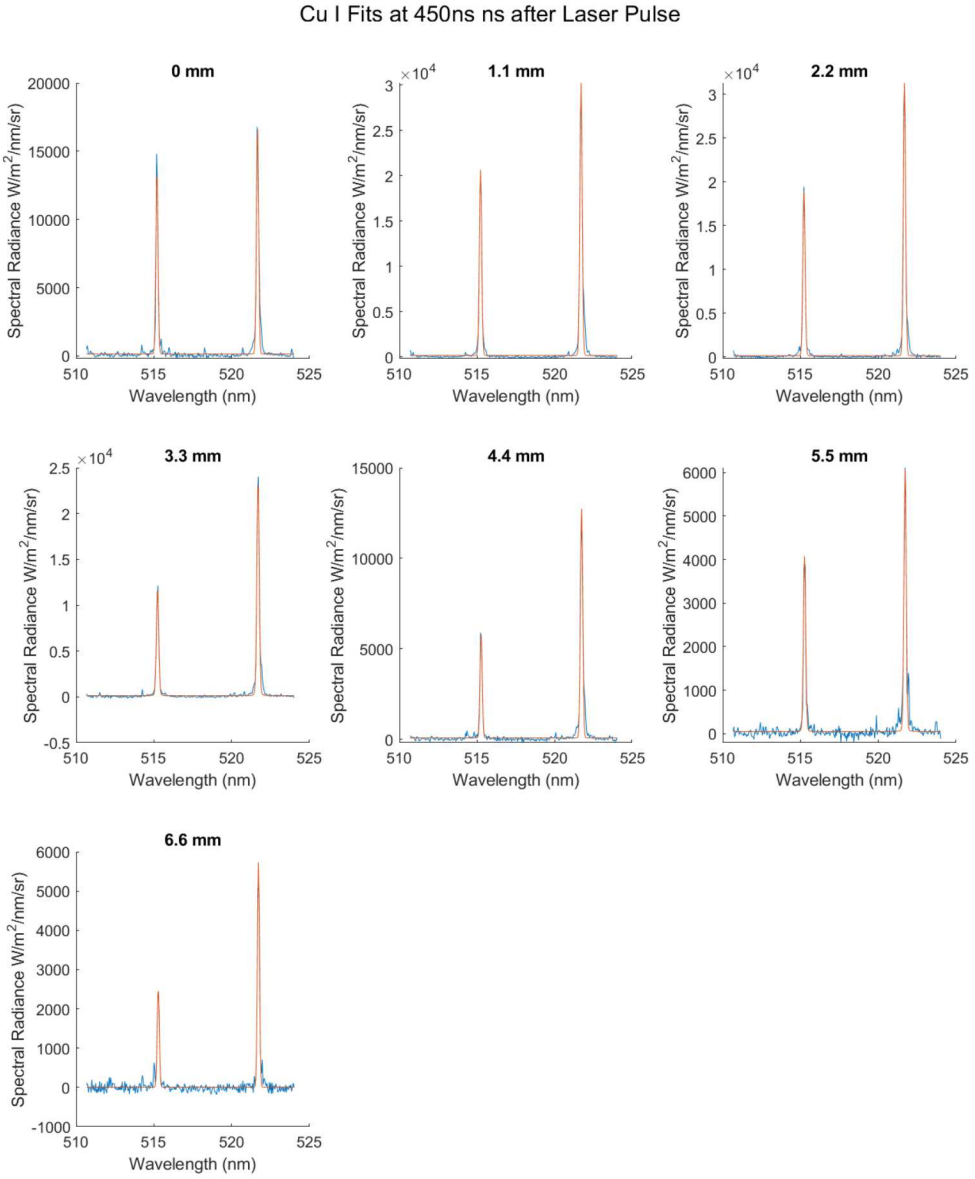

Figure A-29. Cu I fits, 450 ns after laser pulse

Table A-12. Average Lorentzian line widths for Cu I (3d4d-3d4p), only widths greater than 0.03 nm are shown here. Gaussian widths are taken to be the instrument resolution of about 0.17 nm

	100 ns	150ns	200ns	250ns	300 ns	350 ns	400 ns	450 ns
0 mm	0.6692932	0.198492	0.142597					
1.1 mm		0.15	8.43E-02					
2.2 mm			0.071866					
3.3 mm								
4.4 mm								
5.5 mm								
6.6 mm								

Table A-13. Estimated densities from line widths. Assumed Stark Width of 0.054 nm from [6]

	100 ns	150ns	200ns	250ns	300 ns	350 ns	400 ns	450 ns
0 mm	1.22E+17	3.62E+16	2.60E+16					
1.1 mm		2.73E+16	1.54E+16					
2.2 mm			1.31E+16					
3.3 mm								
4.4 mm								
5.5 mm								
6.6 mm								

Table A-14. Peak spectral radiance of Cu I (3d4d-3d4p)

	100 ns	150ns	200ns	250ns	300 ns	350 ns	400 ns	450 ns
0 mm	167469.2711	348888.1	315967.9	118561.6	55797.92	41798.43	23535.23	16764.24
1.1 mm	0	63210.84	96750.53	93602.36	71425.17	57316.9	39434.84	30055.95
2.2 mm	0	0	16617.59	27047.94	43327.03	38674.07	33877.5	31231.37
3.3 mm	0	0	0	8531.249	13513.28	17528.43	20973.63	23678.19
4.4 mm	0	0	0		4045.804	7354.499	9808.959	12755.99
5.5 mm	0	0	0	0	0	4146.775	4757.799	6046.853
6.6 mm	0	0	0	0	0	2198.906	2266.071	5729.847

DISTRIBUTION

Email—Internal

Name	Org.	Sandia Email Address
Technical Library	9536	libref@sandia.gov

Sandia National Laboratories is a multimission laboratory managed and operated by National Technology & Engineering Solutions of Sandia LLC, a wholly owned subsidiary of Honeywell International Inc., for the U.S. Department of Energy's National Nuclear Security Administration under contract DE-NA0003525.